

ACA CO($J = 2 - 1$) Mapping of the Nearest Spiral Galaxy M33. I. Initial Results and Identification of Molecular Clouds

KAZUYUKI MURAOKA,¹

(AAS JOURNALS DATA EDITORS)

AYU KONISHI,¹ KAZUKI TOKUDA,^{2,3,1} HIROSHI KONDO,¹ RIE E. MIURA,^{4,3} TOMOKA TOSAKI,⁵ SACHIKO ONODERA,⁶
NARIO KUNO,^{7,8} MASATO I. N. KOBAYASHI,^{3,9} KISETSU TSUGE,¹⁰ HIDETOSHI SANO,¹¹ NAOYA KITANO,¹ SHINJI FUJITA,^{12,1}
ATSUSHI NISHIMURA,³ TOSHIKAZU ONISHI,¹ KAZUYA SAIGO,¹³ RIN I. YAMADA,¹⁴ FUMIKA DEMACHI,¹⁴ KENGO TACHIHARA,¹⁴
YASUO FUKUI^{14,15} AND AKIKO KAWAMURA³

¹*Department of Physics, Graduate School of Science, Osaka Metropolitan University, 1-1 Gakuen-cho, Naka-ku, Sakai, Osaka 599-8531, Japan*

²*Department of Earth and Planetary Sciences, Faculty of Science, Kyushu University, Nishi-ku, Fukuoka 819-0395, Japan*

³*National Astronomical Observatory of Japan, National Institutes of Natural Science, 2-21-1 Osawa, Mitaka, Tokyo 181-8588, Japan*

⁴*Departamento de Fisica Teorica y del Cosmos, Campus de Fuentenueva, Universidad de Granada, E18071-Granada, Spain*

⁵*Joetsu University of Education, Yamayashiki-machi, Joetsu, Niigata 943-8512, Japan*

⁶*Meisei University, 2-1-1 Hodokubo, Hino, Tokyo 191-0042, Japan*

⁷*Division of Physics, Faculty of Pure and Applied Sciences, University of Tsukuba, 1-1-1 Tennodai, Tsukuba, Ibaraki 305-8577, Japan*

⁸*Tomonaga Center for the History of the Universe, University of Tsukuba, Tsukuba, Ibaraki 305-8571, Japan*

⁹*I. Physikalisches Institut, Universität zu Köln, Zùlpicher Str 77, D-50937 Köln, Germany*

¹⁰*Department of Physics, The University of Tokyo, 7-3-1 Hongo, Bunkyo-ku, Tokyo 113-0033, Japan*

¹¹*Faculty of Engineering, Gifu University, 1-1 Yanagido, Gifu 501-1193, Japan*

¹²*Institute of Astronomy, The University of Tokyo, 2-21-1, Osawa, Mitaka, Tokyo 181-0015, Japan*

¹³*Graduate School of Science and Engineering, Kagoshima University, 1-21-40 Korimoto Kagoshima-city Kagoshima, 890-0065, Japan*

¹⁴*Department of Physics, Nagoya University, Chikusa-ku, Nagoya 464-8602, Japan*

¹⁵*Institute for Advanced Research, Nagoya University, Furo-cho, Chikusa-ku, Nagoya 464-8601, Japan*

(Received; Revised; Accepted)

Submitted to ApJ

ABSTRACT

We present the results of ALMA-ACA 7 m-array observations in $^{12}\text{CO}(J = 2 - 1)$, $^{13}\text{CO}(J = 2 - 1)$, and $\text{C}^{18}\text{O}(J = 2 - 1)$ line emission toward the molecular-gas disk in the Local Group spiral galaxy M33 at an angular resolution of $7''.31 \times 6''.50$ ($30 \text{ pc} \times 26 \text{ pc}$). We combined the ACA 7 m-array $^{12}\text{CO}(J = 2 - 1)$ data with the IRAM 30 m data to compensate for emission from diffuse molecular-gas components. The ACA+IRAM combined $^{12}\text{CO}(J = 2 - 1)$ map clearly depicts the cloud-scale molecular-gas structure over the M33 disk. Based on the ACA+IRAM $^{12}\text{CO}(J = 2 - 1)$ cube data, we cataloged 848 molecular clouds with a mass range from $10^3 M_{\odot}$ to $10^6 M_{\odot}$. We found that high-mass clouds ($\geq 10^5 M_{\odot}$) tend to associate with the $8 \mu\text{m}$ -bright sources in the spiral arm region, while low-mass clouds ($< 10^5 M_{\odot}$) tend to be apart from such $8 \mu\text{m}$ -bright sources and to exist in the inter-arm region. We compared the cataloged clouds with GMCs observed by the IRAM 30 m telescope at 49 pc resolution (IRAM GMC: Corbelli et al. 2017), and found that a small IRAM GMC is likely to be identified as a single molecular cloud even in ACA+IRAM CO data, while a large IRAM GMC can be resolved into multiple ACA+IRAM clouds. The velocity dispersion of a large IRAM GMC is mainly dominated by the line-of-sight velocity difference between small clouds inside the GMC rather than the internal cloud velocity broadening.

Keywords: Interstellar medium(847) — Molecular clouds(1072) — Triangulum Galaxy(1712) – Local Group(929)

1. INTRODUCTION

The interstellar medium (ISM) is one of the crucial components in galaxies because stars are formed by

the contraction of molecular ISM. In the Milky Way (MW), a large fraction of molecular ISM is in the form of giant molecular clouds (GMCs: Sanders et al. 1985), whose typical size and mass are a few $\times 10 - 100$ pc and $10^4 - 10^6 M_\odot$, respectively. It is essential to investigate the properties and formation/evolution processes of GMCs because they are known to be major sites of high-mass star formation, which eventually drives the evolution of galaxies.

So far, a lot of studies have investigated various GMC properties and their relationships. In the MW, Larson (1981) found that the internal velocity dispersions of the molecular clouds are well correlated with their sizes and masses, and also reported that these correlations (i.e., scaling relations) can be expressed as the power-law form. Solomon et al. (1987) measured the velocity dispersions, sizes, virial masses, and CO luminosities for 273 GMCs in the Galactic disk, and found that the velocity dispersion is proportional to the 0.5 power of the size. They also found a tight relationship, over four orders of magnitude, between the virial mass and the CO luminosity with a power-law slope of ~ 0.8 .

Such GMC studies were expanded to the Local Group galaxies outside the MW. Fukui et al. (2008) performed a CO survey toward the Large Magellanic Cloud (LMC) at a spatial resolution of ~ 40 pc, and identified 272 GMCs with a mass range from $2 \times 10^4 M_\odot$ to $7 \times 10^6 M_\odot$ (see also Fukui et al. 1999). In addition, Kawamura et al. (2009) examined spatial comparisons of these GMCs with young star clusters (YSCs) and H II regions and found that the GMCs can be classified into three types: (1) GMCs associated with no H II regions nor YSCs, (2) GMCs associated only with small H II regions, but with no YSCs, and (3) GMCs associated with both YSCs and large H II regions. Such a classification of GMCs according to the activities of high-mass star formation likely reflects their evolutionary sequence. In addition, GMC surveys have been often conducted toward M33, which is one of the nearest spiral galaxies (e.g., Engargiola et al. 2003; Rosolowsky et al. 2007; Gratier et al. 2012; Miura et al. 2012; Corbelli et al. 2017). These studies identified more than 100 GMCs (in particular, more than 500 GMCs by Corbelli et al. 2017) over the M33 disk at ~ 50 pc resolution, and discussed timescales and the evolutionary stages of GMCs based on the comparison with H II regions and YSCs as well as the LMC studies.

High-angular resolution observations by millimeter-wave interferometers enabled to perform the unbiased GMC surveys even toward external spiral galaxies. Colombo et al. (2014) reported the GMC catalog, which contains ~ 1500 individual objects in the grand-design

spiral galaxy M51 at ~ 40 pc resolution using data from the PdBI Arcsecond Whirlpool Survey (Schinnerer et al. 2013). They proposed that large-scale dynamical processes and feedback from high-mass star formation cause environmental variations in the GMC properties and mass distributions, and also suggested that $\sim 30\%$ of GMCs in M51 are unbound. More recently, PHANGS-ALMA survey mapped CO($J = 2 - 1$) line emission at $\sim 1''$ resolution toward 90 nearby star-forming galaxies (Leroy et al. 2021). In particular, Rosolowsky et al. (2021) identified 4986 molecular clouds at a common 90 pc resolution and measured their properties for ten subsamples. They found that the physical properties of clouds vary among galaxies, both as a function of galactocentric radius and as a function of the dynamical environment (e.g., bar, spiral arm, and inter-arm).

However, these earlier studies for external spiral galaxies are likely biased toward the massive ($\geq 10^5 M_\odot$) population of molecular clouds except for the case of M33 (e.g., a small GMC down to $2.4 \times 10^4 M_\odot$ is recovered by Corbelli et al. 2017). To understand the complex hierarchical structures of molecular gas and also to understand the evolution of molecular clouds in galaxies, smaller and less massive ($< 10^5 M_\odot$) molecular clouds should be investigated (e.g., the slope of molecular cloud mass functions changes with evolution processes; Kobayashi et al. 2017, 2018). Thus, we need further molecular-cloud surveys covering such less massive clouds in nearby galaxies as a complementary study to PHANGS-ALMA survey.

In this paper, we present the results of a new CO($J = 2 - 1$) survey toward almost the whole molecular-gas disk of M33 conducted with the Atacama Compact Array (ACA) stand-alone mode of ALMA. The distance to M33 is estimated to be 840 kpc (Freedman et al. 1991; Galletti et al. 2004); thus, $1''$ corresponds to 4 pc. The inclination of M33 is 55° (Koch et al. 2018). Its proximity and relatively small inclination angle have enabled many researchers to study the ISM and high-mass star formation over the wide area of the M33 disk at a few $\times 10$ pc scale (Engargiola et al. 2003; Rosolowsky et al. 2007; Onodera et al. 2010; Gratier et al. 2010; Tosaki et al. 2011; Gratier et al. 2012; Miura et al. 2012; Onodera et al. 2012; Miura et al. 2014; Druard et al. 2014; Gratier et al. 2017; Corbelli et al. 2017). In addition, recent studies based on ALMA 12-m array observations revealed complicated internal molecular-gas structures within some especially massive ($\sim 10^6 M_\odot$) GMCs of M33 at 1–2 pc scale (e.g., Tokuda et al. 2020; Muraoka et al. 2020; Kondo et al. 2021; Sano et al. 2021). Thus, M33 is a unique target to investigate the hierarchical structure of molecular gas in face-on spiral galaxies from parsec

to kiloparsec scales. The basic properties of M33 are summarized in Table 1. The main purposes of the new ACA observations are to obtain the spatial distribution in CO($J = 2 - 1$) emission with the higher sensitivity and higher angular resolution compared to earlier studies in M33 and to identify low-mass ($< 10^5 M_{\odot}$) clouds as well as high-mass ($\geq 10^5 M_{\odot}$) clouds. This surely becomes an important step to understand the hierarchical structures of molecular gas and the evolution of molecular clouds in galaxies.

The structure of this paper is as follows. In Section 2, we describe the detail of the ACA observations and data reduction. Then, we present the overall molecular-gas structures in CO($J = 2 - 1$) emission at ~ 30 pc resolution in M33 in Section 3. In Section 4, we describe the procedure of cloud decomposition based on $^{12}\text{CO}(J = 2 - 1)$ cube data, and summarize the basic properties of cataloged molecular clouds. In Section 5, we examine the scaling relations for the molecular clouds in M33. We compare the cataloged molecular clouds in this study with the earlier GMC catalog in M33 summarized by Corbelli et al. (2017) in Section 6. Finally, we discuss the relationship between the properties of molecular clouds and the high-mass star formation in M33 in Section 7.

2. OBSERVATIONS AND DATA REDUCTION

Observations toward M33 were carried out in Band 6 (211–275 GHz) with the ACA 7 m antennas between 2019 August and 2021 August (project code 2018.A.00058.S). The target molecular lines were $^{12}\text{CO}(J = 2 - 1)$, $^{13}\text{CO}(J = 2 - 1)$, and $\text{C}^{18}\text{O}(J = 2 - 1)$. The bandwidths of the correlator settings were 117.19 MHz with 1920 channels for the ^{12}CO line and 960 channels for ^{13}CO and C^{18}O lines. The target field was the rectangle with the size of $1100'' \times 1180''$ ($4.5 \text{ kpc} \times 4.8 \text{ kpc}$), covering most of the molecular-gas disk of M33. The total number of mosaic fields is 3129. In addition to this, we retrieved the ALMA archival data (project code 2017.1.00901.S and 2019.1.01182.S), which also observed the molecular-gas disk of M33 by ACA 7 m antennas with almost the same spectral settings as our observations. Prior to the imaging process, we concatenated all visibilities obtained in each science goal with a total number of 36. This data reduction strategy is the same as the previously published large-scale ACA mapping project on the Small Magellanic Cloud (SMC) (Tokuda et al. 2021). Figure 1 shows the eventually observed field.

We used Common Astronomy Software Application (CASA) package (McMullin et al. 2007) version 5.4.0 in the data reduction. We applied the standard calibration scheme provided by the ALMA observatory while we performed the imaging process. We used the `tclean` task with `multi-scale` deconvolver (Kepley et al. 2020) to recover extended emission as much as possible. In `tclean` task, we applied the natural weighting and used the `auto-multithresh` procedure to identify automatically regions containing emission in the dirty and residual images. We continued the deconvolution process until the intensity of the residual image attains the $\sim 1\sigma$ noise level. The beam size and the rms noise level for each emission are summarized in Table 2.

To evaluate the missing flux of the ACA observations, we measured the global $^{12}\text{CO}(J = 2 - 1)$ luminosities over the M33 disk obtained by the ACA 7 m antennas and by the IRAM 30 m telescope (Druard et al. 2014). We found the global $^{12}\text{CO}(J = 2 - 1)$ luminosity with ACA 7 m antennas $L_{\text{CO}}^{\text{ACA}} = 7.6 \times 10^6 \text{ K km s}^{-1} \text{ pc}^2$ over the observed region, and that with the IRAM 30 m telescope $L_{\text{CO}}^{\text{IRAM}} = 2.1 \times 10^7 \text{ K km s}^{-1} \text{ pc}^2$ for the same area. This indicates the global missing flux of $^{12}\text{CO}(J = 2 - 1)$ emission of 60 – 70%, which mainly corresponds to diffuse components of molecular gas. To compensate for such diffuse components, we combined the ACA 7 m-array $^{12}\text{CO}(J = 2 - 1)$ data with the IRAM 30 m data using the `feather` task. Hereafter, we refer to the pre-combined ACA 7 m-array $^{12}\text{CO}(J = 2 - 1)$ data as “stand-alone ACA $^{12}\text{CO}(J = 2 - 1)$ ” data, and to the combined $^{12}\text{CO}(J = 2 - 1)$ data as “ACA+IRAM $^{12}\text{CO}(J = 2 - 1)$ ” data. The beam size and the rms noise level of ACA+IRAM $^{12}\text{CO}(J = 2 - 1)$ data are the same as those of the stand-alone ACA $^{12}\text{CO}(J = 2 - 1)$ data.

3. CO MAPS

From the reduced three-dimensional cube data, we examine the zeroth moment (i.e., velocity-integrated intensity) in $^{12}\text{CO}(J = 2 - 1)$ and $^{13}\text{CO}(J = 2 - 1)$ emission. To minimize the effect of the noise, we determined the velocity channel in which the CO emission is expected to appear using the atomic (HI) data (Koch et al. 2018) as follows. Firstly, we convolved the HI data whose original angular resolution is $20''$ to $40''$ in order to reduce the effect of the anomalous HI velocity components. Then, we regridded them to match our CO data and determined the representative HI velocity V_{rep} in each pixel. Finally, we calculated the zeroth moment in $^{12}\text{CO}(J = 2 - 1)$ emission from $V_{\text{rep}} - 30 \text{ km s}^{-1}$ to $V_{\text{rep}} + 30 \text{ km s}^{-1}$. Although Rosolowsky et al. (2007)

Table 1. General properties of M33

Parameter	Value	Reference
IR center (J2000):		(1)
Right Ascension	1 ^h 33 ^m 50 ^s .9	
Declination	30°39'37"	
Distance	840 kpc	(2), (3)
LSR velocity	170 km s ⁻¹	(4)
Inclination	55°	(5)
Position angle	21°	(5)
Stellar mass	4.8 × 10 ⁹ M _⊙	(6)
Molecular gas mass	3.1 × 10 ⁸ M _⊙	(4)

NOTE—References. (1) Skrutskie et al. (2006), (2) Freedman et al. (1991), (3) Galleti et al. (2004), (4) Druard et al. (2014), (5) Koch et al. (2018), (6) Corbelli et al. (2014)

Table 2. Properties of each line emission

Line	Beam Size	Rms Noise Level	Velocity Resolution
¹² CO(<i>J</i> = 2 – 1)	7''31 × 6''50 (30 pc × 26 pc)	39 mK	0.7 km s ⁻¹
¹³ CO(<i>J</i> = 2 – 1)	7''72 × 6''86 (31 pc × 27 pc)	30 mK	1.4 km s ⁻¹
C ¹⁸ O(<i>J</i> = 2 – 1)	7''82 × 6''96 (31 pc × 28 pc)	22 mK	1.6 km s ⁻¹

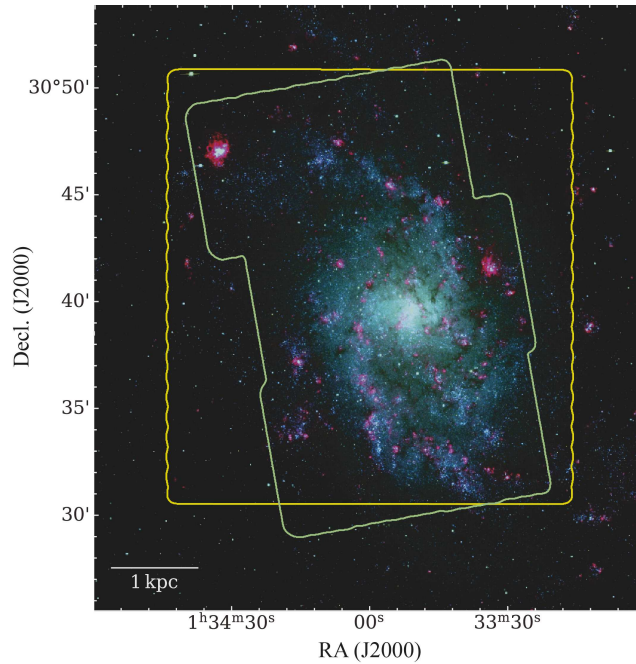


Figure 1. Three-color composite image constructed from the B-band (blue), V-band (green), and H α (red) images of M33 taken with the Mayall 4 m telescope (Massey et al. 2006, 2007). The yellow line indicates the observed field of the project code 2018.A.00058.S, and the green line indicates that of 2017.1.00901.S and 2019.1.01182.S.

reported that 90% of the velocity separation between CO and HI is within 20 km s⁻¹, each CO line typically

has a velocity width of $5\text{--}10\text{ km s}^{-1}$. In fact, we found that some molecular clouds dropped $\sim 30\%$ of CO flux if we apply the velocity range of $V_{\text{rep}} \pm 20\text{ km s}^{-1}$. To correctly measure the CO intensity in M33, we needed the velocity range of $V_{\text{rep}} \pm 30\text{ km s}^{-1}$ for the calculation of the $^{12}\text{CO}(J = 2 - 1)$ zeroth moment. We also calculated the $^{13}\text{CO}(J = 2 - 1)$ zeroth moment from $V_{\text{rep}} - 30\text{ km s}^{-1}$ to $V_{\text{rep}} + 30\text{ km s}^{-1}$.

Figure 2 shows the integrated intensity maps in $^{12}\text{CO}(J = 2 - 1)$ from the stand-alone ACA data and the ACA+IRAM data, respectively. These $^{12}\text{CO}(J = 2 - 1)$ maps clearly depict the molecular-gas structure within M33 at 30 pc resolution. We can easily find a lot of individual molecular clouds over the M33 disk. The ACA+IRAM $^{12}\text{CO}(J = 2 - 1)$ map properly recovers diffuse components of molecular gas, which are missed in the stand-alone ACA map. We show an evident case, $^{12}\text{CO}(J = 2 - 1)$ integrated intensity map for GMCs associated with the giant H II region NGC 604, in Figure 3.

The integrated intensity map in $^{13}\text{CO}(J = 2 - 1)$ emission over the M33 disk is shown in the left panel of Figure 4. A lot of $^{13}\text{CO}(J = 2 - 1)$ sources are detected. They correspond to moderately dense gas whose density is $\gtrsim 10^3\text{ cm}^{-3}$ within the ^{12}CO cloud. The zoomed-in view of the NGC 604 region is shown in the right panel of Figure 4.

Note that we found no significant $\text{C}^{18}\text{O}(J = 2 - 1)$ emission in the ACA map. The rms noise level of 22 mK yields a 3σ upper limit of 66 mK. To check the validity of the upper limit, we retrieved the ALMA archival data (project code 2017.1.00461.S) and examined the $\text{C}^{18}\text{O}(J = 2 - 1)$ emission in a GMC associated with NGC 604. We found that the peak temperature of the strongest $\text{C}^{18}\text{O}(J = 2 - 1)$ emission is $\sim 1\text{ K}$ at an angular resolution of $0''.3$ (1.2 pc) and its spatial extent is less than $1''$. Then, we convolved the $\text{C}^{18}\text{O}(J = 2 - 1)$ emission to $7''.5$ and found that the peak temperature decreases down to $\sim 30\text{ mK}$, which corresponds to 1.4σ in the ACA $\text{C}^{18}\text{O}(J = 2 - 1)$ map. Thus, we consider that the beam smearing effect makes $\text{C}^{18}\text{O}(J = 2 - 1)$ emission undetectable in the ACA 30 pc-resolution map.

4. CLOUD DECOMPOSITION

As shown in Figure 2, the structure of molecular clouds is highly complex and hierarchical over the M33 disk. To identify individual emission structures in an objective way and to investigate the properties of molecular clouds, we employed PYCPROPS (Rosolowsky et al. 2021), a Python implementation of the algorithm to catalog molecular clouds, CPROPS (Rosolowsky & Leroy 2006). We use the ACA+IRAM $^{12}\text{CO}(J = 2 - 1)$ data in the following analyses.

Firstly, we convolved the ACA+IRAM $^{12}\text{CO}(J = 2 - 1)$ cube data to $7''.5$ in order to identify molecular clouds by a circular beam. Then, we made masked cube data using `cprops_mask` provided by Rosolowsky et al. (2021). The criteria of the emission mask are that high significance emission is required to be more than 4σ in continuous three velocity channels and low significance emission which is adjacent to high significance emission is required to be more than 3σ in continuous three velocity channels at least over the size of the ACA $7''.5$ beam. Although the default settings of `cprops_mask` are 4σ and 2σ for high and low significance masks, respectively, we found that the emission masks with these default settings are not suitable for the ACA+IRAM $^{12}\text{CO}(J = 2 - 1)$ cube data. In particular, the low significance mask does not reject fake emission (i.e., noise) at the cloud edge. Thus, we carefully tuned the rms thresholds, and finally we adopted 3σ for low significance masks.

PYCPROPS firstly searches for all local maxima in the emission-masked cube data and measures the peak temperature in each local maximum, T_{max} . When a local maximum has at least one other neighbor whose peak temperature is T_{merge} , PYCPROPS compares T_{max} and T_{merge} . The neighbor is rejected if $T_{\text{max}} - T_{\text{merge}}$ is less than 2σ , which means that such a local maximum is likely a noise fluctuation. The criterion of 2σ is a default value recommended by Rosolowsky et al. (2008). Then, PYCPROPS determines if the spatial and spectral separations between local maxima are adequate or not. We adopted the beam size ($7''.5$) as a minimum spatial separation and also adopted 7 km s^{-1} as a minimum spectral separation, which corresponds to a typical velocity width of a GMC with the size of $\sim 30\text{ pc}$ considering the Galactic size-linewidth relation (Solomon et al. 1987). If either spatial separation or spectral separation between local maxima does not satisfy the above threshold, the local maximum which has a smaller T_{max} is rejected. Through these processes, PYCPROPS identifies a set of significant local maxima. We treat these local maxima as seeds to assign all the emission to molecular clouds. To do this, we use a watershed algorithm, which associates all the cube pixels in the emission-masked data with a local maximum. Some pixels are already assigned to a single local maximum, while the remainder (including rejected local maxima in the above processes) are assigned to any of the local maxima by the watershed algorithm. More details on the PYCPROPS algorithm are summarized in Rosolowsky et al. (2021). Finally, PYCPROPS identified 886 molecular clouds.

PYCPROPS gives the basic properties of the identified clouds, including the extrapolated 2nd moment of the

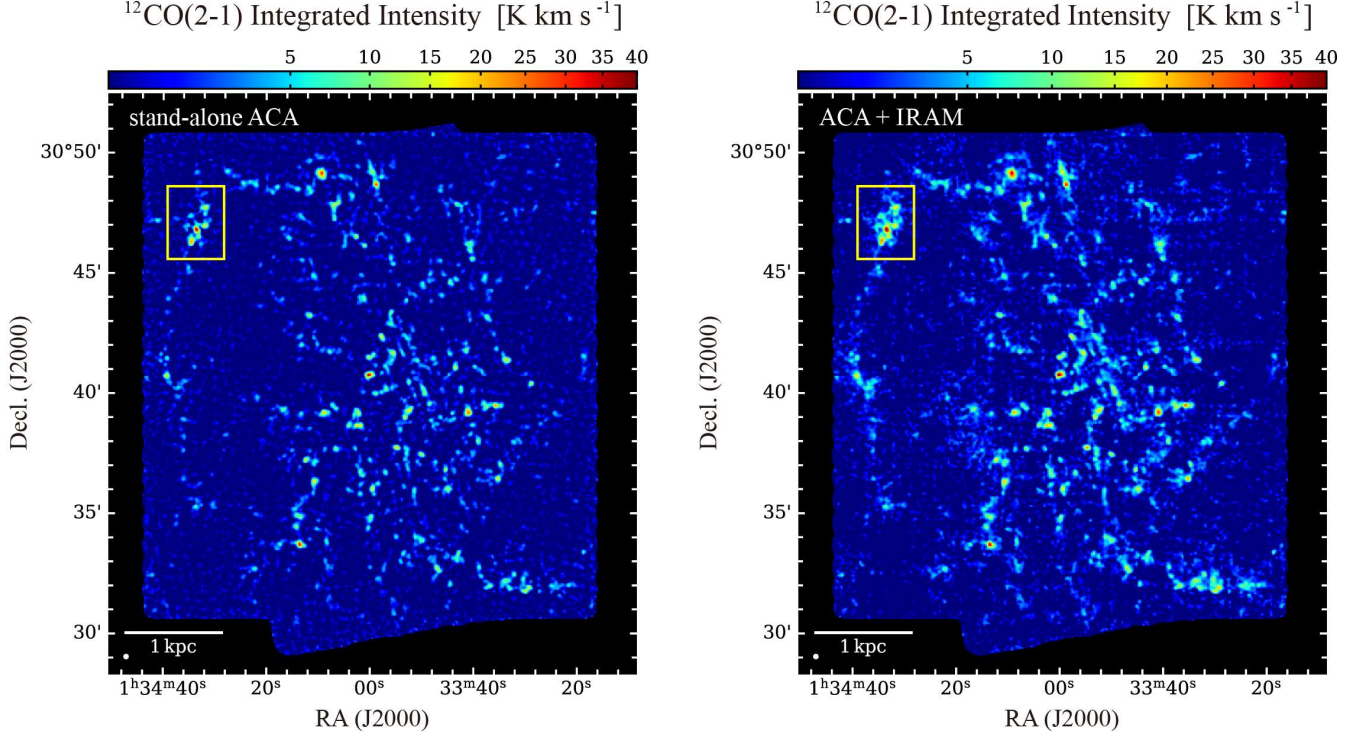


Figure 2. Integrated intensity maps in $^{12}\text{CO}(J = 2 - 1)$ from the stand-alone ACA data (left) and the ACA+IRAM data (right). The yellow rectangle indicates the NGC 604 region. A zoomed-in view of this region is shown in Figure 3. The synthesized beam is shown in the lower left corner.

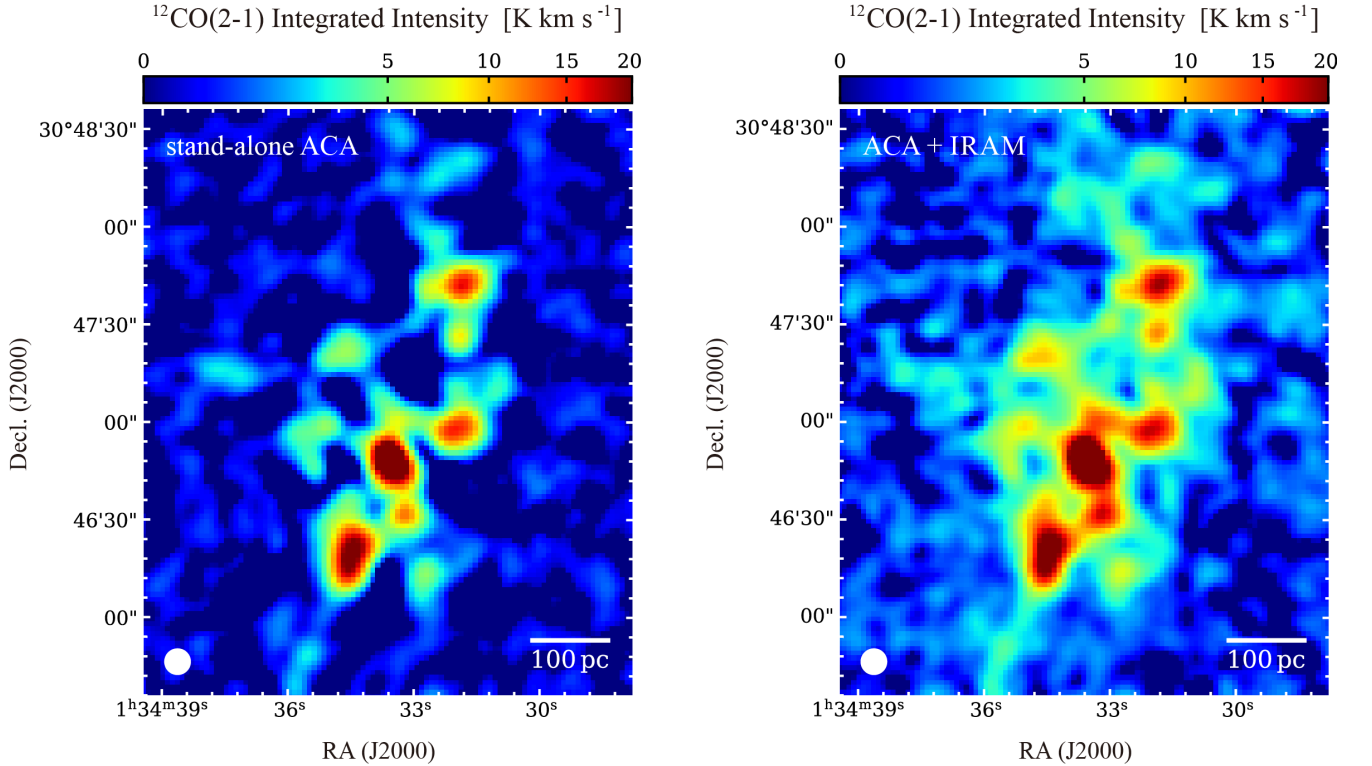


Figure 3. Zoomed-in view of the NGC 604 region in Figure 2. Diffuse molecular-gas components between bright GMCs are well recovered. The synthesized beam is shown in the lower left corner.

emission along the major and minor axes σ_{maj} and σ_{min}

in parsec, the position angle of the major axis ϕ , the ex-

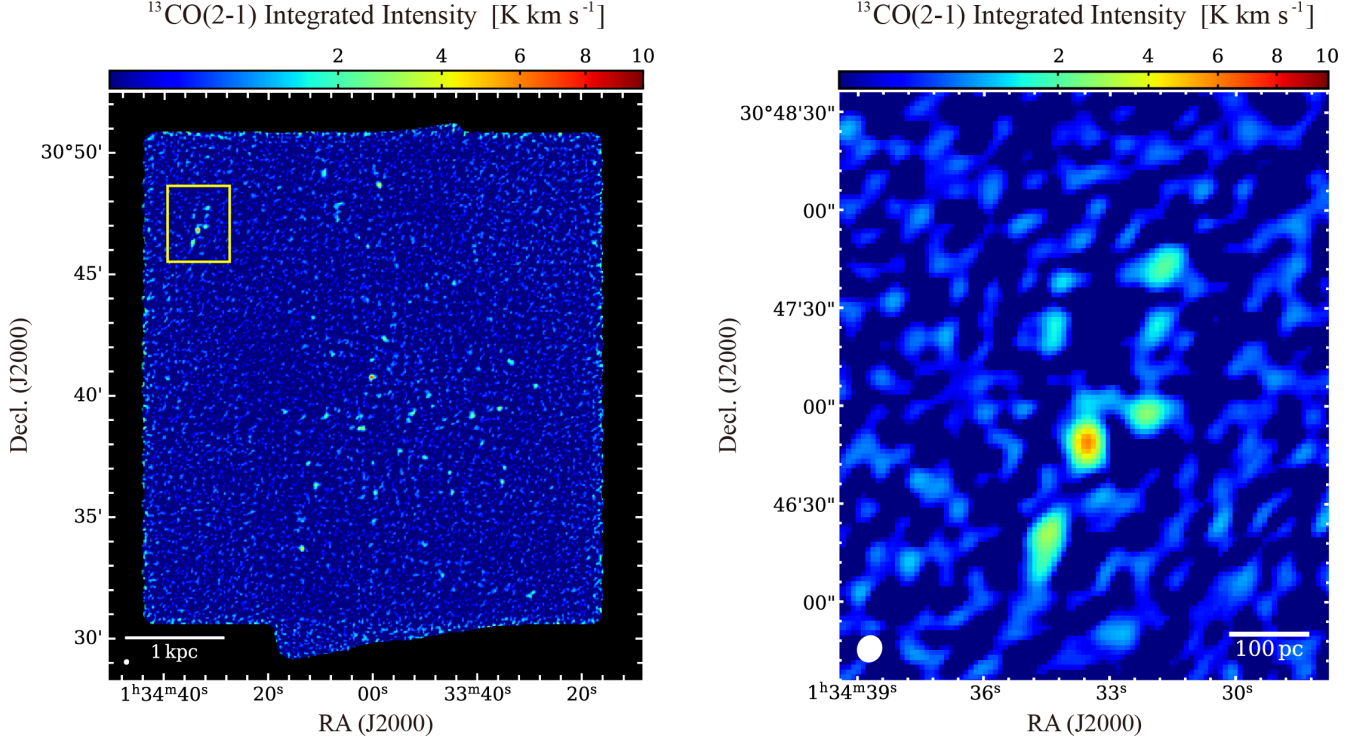


Figure 4. Integrated intensity map in $^{13}\text{CO}(J=2-1)$ emission of M33 obtained by the ACA 7 m-array (left) and its zoomed-in view of the NGC 604 region (right). The synthesized beam is shown in the lower left corner.

trapolated velocity dispersion $\sigma_{v,\text{ext}}$, and the integrated $^{12}\text{CO}(J=2-1)$ flux S within each cloud. The extrapolated cloud properties are calculated to reduce observational bias (Rosolowsky & Leroy 2006). In Figure 5, we showed frequency distributions of the ratio between the extrapolated value and the observed value for cloud size and velocity dispersion. The extrapolated value is typically 10–20% larger than the observed value.

We calculated the intrinsic spherical radius R by the deconvolution of the ACA+IRAM beam, σ_{beam} , as follows:

$$R = 1.91 \sqrt{(\sigma_{\text{maj}}^2 - \sigma_{\text{beam}}^2)^{0.5} (\sigma_{\text{min}}^2 - \sigma_{\text{beam}}^2)^{0.5}}. \quad (1)$$

Here, σ_{beam} is calculated as $7''.5 \times 4 = 30''$, where the factor of 4 is the spatial size in parsec of $1''$ at the distance of M33 (840 kpc). The coefficient 1.91 converts the rms size to the effective spherical radius of the cloud (e.g., Solomon et al. 1987; Rosolowsky & Leroy 2006). We treat R as the intrinsic spherical radius of each molecular cloud. Note that if σ_{min} is smaller than σ_{beam} , the resultant R is not properly defined. We do not consider such small clouds further in this paper.

We also deconvolved the velocity dispersion $\sigma_{v,\text{ext}}$ as follows:

$$\sigma_v = \sqrt{\sigma_{v,\text{ext}}^2 - \frac{\sigma_{v,\text{chan}}^2}{2\pi}}, \quad (2)$$

where $\sigma_{v,\text{chan}}$ is the velocity resolution element, which is related to the velocity channel width ($\Delta V_{\text{chan}} = 0.7 \text{ km s}^{-1}$) as $\sigma_{v,\text{chan}} = \Delta V_{\text{chan}} / (2\sqrt{2 \ln 2})$.

We do not consider molecular clouds lying at the edge of the ACA field-of-view (FOV) further because the primary beam correction causes larger uncertainties in the obtained properties of molecular clouds. Thus, we consider 848 molecular clouds after excluding small clouds with undefined radius and clouds at the edge of ACA FOV from the originally identified clouds by PYCPROPS. Figure 6 shows the spatial distribution of 848 molecular clouds, whose deconvolved sizes and the measured position angle are represented, in the M33 disk.

4.1. Luminosities and Masses

From the basic properties of molecular clouds, we calculated additional properties such as the CO luminosity $L_{\text{CO}} = SD^2$ where $D = 840 \text{ kpc}$ and cloud masses. The luminosity-based mass (for ^{12}CO , hereafter M_{CO}) which includes the helium contribution is calculated as

$$\frac{M_{\text{CO}}}{M_{\odot}} = 4.35 \frac{X_{\text{CO}}}{2.0 \times 10^{20} \text{ cm}^{-2} (\text{K km s}^{-1})^{-1}} \frac{L_{\text{CO}}}{\text{K km s}^{-1} \text{ pc}^2} R_2 \sqrt{\frac{3}{4}} \quad (3)$$

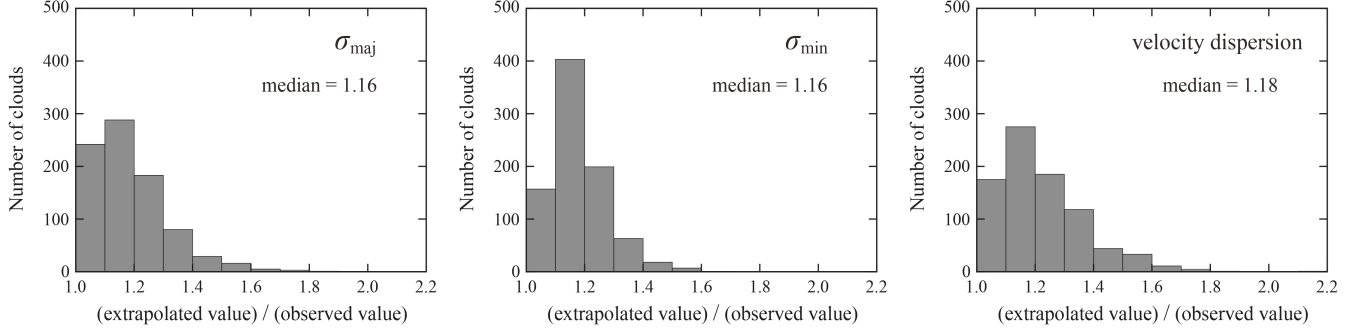


Figure 5. Frequency distributions of the ratio between the extrapolated value and the observed value for the second moment of the major axis (σ_{maj} ; left), that of the minor axis (σ_{min} ; center), and velocity dispersion (right), respectively.

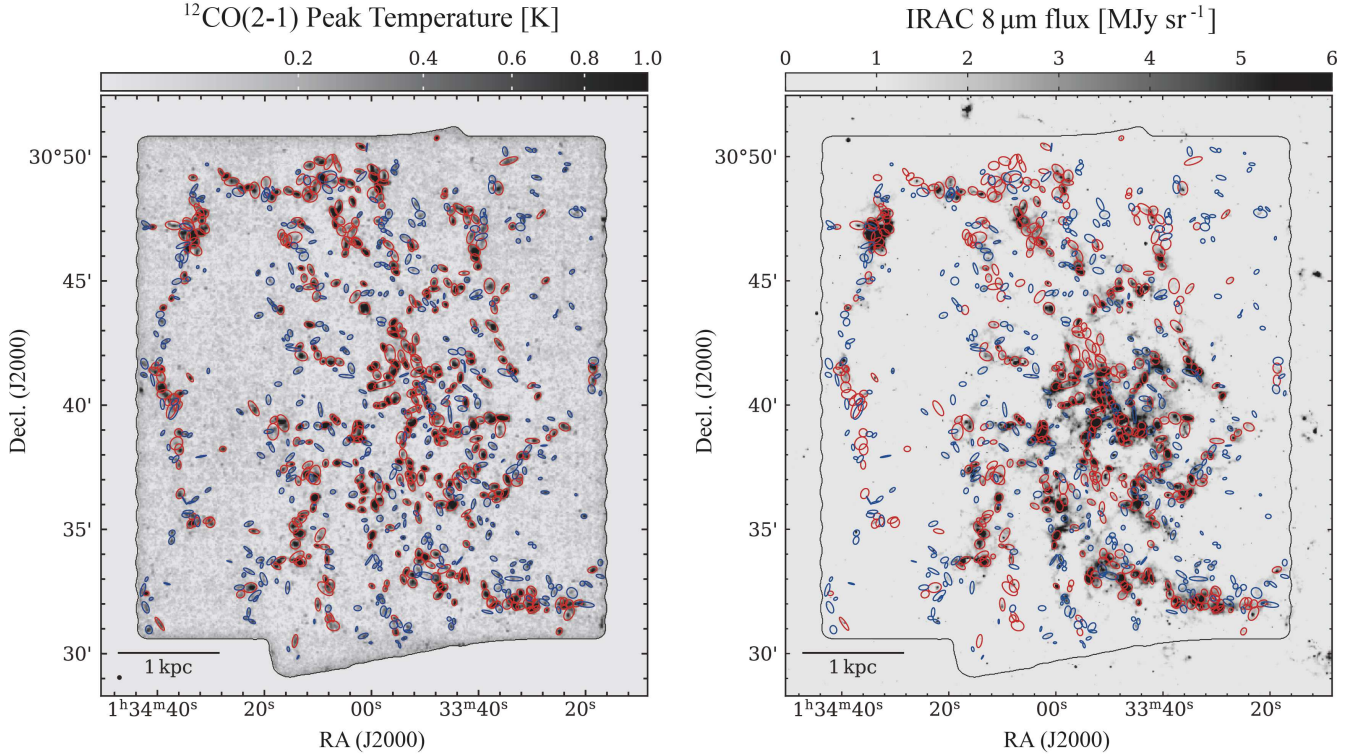


Figure 6. Distribution of 848 molecular clouds in M33 superposed on the ACA+IRAM combined $^{12}\text{CO}(J = 2 - 1)$ peak temperature map (left) and the map of *Spitzer*/IRAC $8\ \mu\text{m}$ flux obtained by Dale et al. (2009) (right). The molecular clouds are represented as ellipses, whose sizes and orientation indicate the extrapolated and deconvolved major and minor axes, and the measured position angle. Red ellipses represent high-mass clouds ($M_{\text{CO}} \geq 10^5 M_{\odot}$) and blue ellipses indicate low-mass clouds ($M_{\text{CO}} < 10^5 M_{\odot}$). The black line indicates the eventually observed field by ACA.

where X_{CO} is CO-to- H_2 conversion factor and R_{21} is the $^{12}\text{CO}(J = 2 - 1)/^{12}\text{CO}(J = 1 - 0)$ intensity ratio. We adopted a constant X_{CO} of $4.0 \times 10^{20}\ \text{cm}^{-2}\ (\text{K km s}^{-1})^{-1}$ (Gratier et al. 2017) over the M33 disk. To determine the appropriate R_{21} value in this study, we examined the pre-existing single-dish measurements of ^{12}CO in M33 for $J = 1 - 0$ (Tosaki et al. 2011) and $J = 2 - 1$ (Gratier et al. 2010; Druard et al. 2014) transitions. We found that the average R_{21} in M33 is 0.60, but this value is lower than the previously-reported R_{21} of 0.8 (Druard et al. 2014). In the MW, the reported

R_{21} is 0.64 (Yoda et al. 2010). In addition, recent studies reported that the mean of R_{21} in nearby galaxies is 0.6–0.7 (e.g., Yajima et al. 2021; den Brok et al. 2021; Leroy et al. 2022). These R_{21} values are consistent with the newly-obtained one in M33, 0.60. Thus, we adopted a constant $R_{2-1/1-0}$ of 0.60 across the M33 disk in this study. Note that, as pointed out by Yajima et al. (2021), R_{21} varies within an individual galaxy; in fact, R_{21} in M33 varies from position to position, typically ranging from 0.4 to 0.8. Therefore we consider that the assumption of a constant $R_{2-1/1-0}$ over the M33 disk yields

an error of about 30%. From the emission masks and PYCPROPS parameters, the detection limit of M_{CO} is calculated to be $3 \times 10^3 M_{\odot}$, while the actual lowest mass of the molecular clouds is $7 \times 10^3 M_{\odot}$.

In Figure 6, each molecular cloud is color-coded according to its M_{CO} , i.e., red ellipses represent high-mass clouds ($M_{\text{CO}} \geq 10^5 M_{\odot}$) and blue ellipses indicate low-mass clouds ($M_{\text{CO}} < 10^5 M_{\odot}$). In addition, the spatial comparison between molecular clouds and *Spitzer*/IRAC $8 \mu\text{m}$ emission (Dale et al. 2009) is displayed. In the spiral arm region, many high-mass clouds are associated with the strong (typically $> 2 \text{ MJy sr}^{-1}$) $8 \mu\text{m}$ emission, which likely traces high-mass star-forming regions (e.g., Calzetti et al. 2005; Wu et al. 2005; Calzetti et al. 2007; Crocker et al. 2013). On the other hand, low-mass clouds tend to be apart from such $8 \mu\text{m}$ -bright sources and to exist in the inter-arm region.

We examine the mass fraction of the molecular clouds to the total molecular gas over the ACA-observed area. The total mass of the molecular clouds is derived to be $1.6 \times 10^8 M_{\odot}$ by summing up their M_{CO} values. We calculated the global ACA+IRAM $^{12}\text{CO}(J = 2 - 1)$ of $2.0 \times 10^7 \text{ K km s}^{-1} \text{ pc}^2$, which yields the total molecular gas mass of $2.9 \times 10^8 M_{\odot}$ ¹. Thus, the mass fraction of molecular clouds to the total molecular gas is 55%. This is similar to the case in M51; Pety et al. (2013) reported that about half of the CO luminosity arises from molecular clouds and the other half from diffuse components of molecular gas.

We also calculated the virial mass as $M_{\text{vir}} = 1040 R \sigma_v^2$ for a spherical and virialized cloud with a density profile of $\rho \propto r^{-1}$ (Bolatto et al. 2013). Its relationship with M_{CO} is discussed in Section 5.

4.2. $^{13}\text{CO}(J = 2 - 1)$ Emission

We examined $^{13}\text{CO}(J = 2 - 1)$ emission for each cloud. The criteria for the “detection” of $^{13}\text{CO}(J = 2 - 1)$ emission are as follows. Firstly, we drew the $^{12}\text{CO}(J = 2 - 1)$ spectrum at the $^{12}\text{CO}(J = 2 - 1)$ peak of each cloud and defined the “line channels”, which are successive velocity channels where significant $^{12}\text{CO}(J = 2 - 1)$ emission exists. Then, we examined the $^{13}\text{CO}(J = 2 - 1)$ spectrum within the line channels. If $^{13}\text{CO}(J = 2 - 1)$ emission exceeds 4σ for successive 2 channels or exceeds 3σ for successive 3 channels, we treat the $^{13}\text{CO}(J = 2 - 1)$

emission as temporarily-detected. In addition, we calculated the $^{13}\text{CO}(J = 2 - 1)$ integrated intensity within the line channels, and derive its signal-to-noise (S/N) ratio. If the S/N ratio of the temporarily-detected $^{13}\text{CO}(J = 2 - 1)$ intensity exceeds 3, we finally treat the $^{13}\text{CO}(J = 2 - 1)$ emission as significantly detected. We confirmed significant $^{13}\text{CO}(J = 2 - 1)$ emission for 173 clouds, and thus the resultant $^{13}\text{CO}(J = 2 - 1)$ detection rate is 20%.

We examined the $^{13}\text{CO}(J = 2 - 1)/^{12}\text{CO}(J = 2 - 1)$ intensity ratio (hereafter $R_{13/12}$) for the $^{13}\text{CO}(J = 2 - 1)$ detected clouds. We found that $R_{13/12}$ in M33 is almost constant on the galactocentric radius as shown in Figure 7, and the typical $R_{13/12}$ is ~ 0.1 . This value is similar to that in the disk of M51 (den Brok et al. 2022), and also similar to that for $J = 1 - 0$ transition (i.e., $^{13}\text{CO}(J = 1 - 0)/^{12}\text{CO}(J = 1 - 0)$ ratio) measured in nearby galaxy disks (e.g., Paglione et al. 2001; Hirota et al. 2010; Watanabe et al. 2011; Muraoka et al. 2016; Cao et al. 2017; Cormier et al. 2018; Yajima et al. 2019; Topal 2020; Morokuma-Matsui et al. 2020; Cao et al. 2023).

4.3. Catalog Description

We summarized the properties of 848 clouds in M33 as a catalog, which do not include small clouds with undefined radius and clouds at the edge of ACA FOV. We assigned the ID number of the clouds in order of increasing the galactocentric radius. Table 3 presents the first 10 and last 10 clouds of the catalog, and the full version is available online.

The uncertainty of each property was evaluated using a bootstrapping method implemented in PYCPROPS. Considering that the cloud consists of N data points, we generated a trial cloud by N times random sampling of the data allowing the same data to be sampled more than once. Then, we measured the properties of the trial cloud. We repeated the resampling and remeasuring 10,000 times for each cloud, and evaluated the uncertainties. The final uncertainty in each property is the median absolute deviation of the bootstrapped values scaled up by the square root of the over-sampling rate, which corresponds to the number of pixels per beam size. This scaling accounts for the fact that pixels within the same beam are not independent (i.e., correlated with each other).

In this molecular-cloud catalog, we noted the S/N ratio of $^{12}\text{CO}(J = 2 - 1)$ brightness temperature at the CO peak position in each GMC. As reported in Rosolowsky & Leroy (2006), the CPROPS algorithm requires a minimum S/N ratio of 10 for stable recovery of cloud properties. Since our catalog includes 147 molec-

¹ The $^{12}\text{CO}(J = 2 - 1)$ data obtained by IRAM 30 m telescope (Druard et al. 2014) gives its luminosity of $2.1 \times 10^7 \text{ K km s}^{-1} \text{ pc}^2$ within the ACA FOV (see Section 2). If we assume X_{CO} of $4.0 \times 10^{20} \text{ cm}^{-2} (\text{K km s}^{-1})^{-1}$ and R_{21} of 0.6, this luminosity yields the total molecular gas mass of $3.0 \times 10^8 M_{\odot}$, which is well consistent with the molecular gas mass of $2.9 \times 10^8 M_{\odot}$ derived from ACA+IRAM $^{12}\text{CO}(J = 2 - 1)$ data.

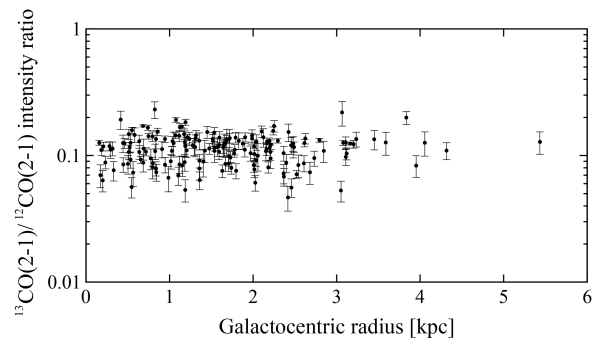


Figure 7. $^{13}\text{CO}(J = 2 - 1)/^{12}\text{CO}(J = 2 - 1)$ intensity ratio ($R_{13/12}$) as a function of the galactocentric radius for the $^{13}\text{CO}(J = 2 - 1)$ detected clouds in M33.

ular clouds whose S/N ratio is lower than 10, we examine the properties of such low-S/N clouds in the following analyses. The minimum S/N ratio of the cataloged

cloud is 6.1. In addition, we checked a GMC counterpart identified with the IRAM 30 m telescope (Corbelli et al. 2017). We make a comparison between the two catalogs in Section 6.

Table 3. List of cataloged molecular clouds

ID	R.A.	Decl.	R_{gal}	V_{LSR}	R	σ_v	M_{CO}	M_{vir}	$I_{12\text{CO}}$	^{12}CO S/N	$I_{13\text{CO}}$	$R_{13/12}$	ϕ	b/a	IRAM ID
(1)	(deg.)	(deg.)	(kpc)	(km s^{-1})	(pc)	(km s^{-1})	($10^4 M_{\odot}$)	($10^4 M_{\odot}$)	(K km s^{-1})	(11)	(K km s^{-1})	(13)	($^{\circ}$)	(15)	(16)
1	23.46415	30.65744	0.07	-168	17.3 ± 4.4	3.7 ± 0.9	3.8 ± 2.0	24.2 ± 8.6	1.83 ± 0.08	10.0	< 0.36	< 0.20	24	5.0	149
2	23.46366	30.66494	0.07	-202	29.2 ± 4.2	4.6 ± 0.6	16.5 ± 3.3	64.4 ± 12.0	6.50 ± 0.13	18.2	< 0.35	< 0.05	-75	2.1	
3	23.46754	30.66369	0.10	-187	46.3 ± 10.2	2.5 ± 0.5	10.2 ± 4.5	30.8 ± 8.8	2.76 ± 0.12	10.6	< 0.32	< 0.11	25	3.3	156
4	23.45834	30.65327	0.11	-162	19.0 ± 6.9	2.9 ± 0.9	2.5 ± 1.6	16.7 ± 7.8	1.46 ± 0.06	12.4	< 0.25	< 0.17	-61	1.4	
5	23.46560	30.66952	0.14	-203	38.1 ± 3.9	2.9 ± 0.4	18.7 ± 3.8	32.4 ± 6.1	3.61 ± 0.09	22.3	< 0.47	< 0.13	-62	2.0	177
6	23.46754	30.65494	0.16	-168	48.2 ± 2.5	4.0 ± 0.2	125.4 ± 6.9	78.4 ± 5.1	20.94 ± 0.10	95.8	2.64 ± 0.11	0.13 ± 0.01	36	1.2	149
7	23.45495	30.65035	0.17	-163	12.6 ± 10.9	2.4 ± 1.0	1.1 ± 0.1	7.5 ± 5.2	1.20 ± 0.07	7.5	< 0.20	< 0.17	41	4.2	
8	23.45301	30.65869	0.17	-165	35.7 ± 3.4	2.4 ± 0.2	18.7 ± 2.6	21.8 ± 3.1	7.37 ± 0.07	41.3	0.52 ± 0.11	0.07 ± 0.01	-86	2.3	151
9	23.45543	30.66535	0.18	-177	39.4 ± 6.7	4.6 ± 0.7	9.2 ± 0.5	88.4 ± 18.4	2.62 ± 0.10	14.9	< 0.39	< 0.15	-27	1.3	160
10	23.45494	30.66452	0.18	-187	25.9 ± 6.0	2.0 ± 0.5	3.7 ± 2.2	10.5 ± 4.0	3.15 ± 0.09	13.5	< 0.23	< 0.07	-64	1.9	160
...
...
839	23.65535	30.58110	4.69	-174	29.5 ± 8.8	2.5 ± 0.5	7.6 ± 3.3	19.4 ± 5.5	3.00 ± 0.12	12.0	< 0.37	< 0.12	43	1.2	326
840	23.65583	30.57610	4.74	-176	32.2 ± 6.8	2.2 ± 0.3	8.7 ± 3.5	16.7 ± 4.0	3.47 ± 0.09	19.3	< 0.33	< 0.10	69	1.5	326
841	23.65965	30.54693	5.05	-154	13.3 ± 9.3	1.8 ± 0.8	1.7 ± 1.1	4.5 ± 3.2	1.38 ± 0.10	7.1	< 0.18	< 0.13	-15	5.7	
842	23.66347	30.51901	5.36	-152	38.6 ± 6.4	2.7 ± 0.4	13.2 ± 4.8	30.0 ± 6.7	2.49 ± 0.09	16.5	< 0.34	< 0.14	-56	3.9	252
843	23.67514	30.54941	5.36	-165	17.2 ± 10.2	1.8 ± 0.7	1.7 ± 1.8	5.5 ± 3.7	1.08 ± 0.07	8.0	< 0.35	< 0.33	62	2.0	
844	23.67173	30.53649	5.39	-161	16.7 ± 8.7	1.8 ± 0.6	1.8 ± 0.9	5.6 ± 3.2	1.25 ± 0.08	9.3	< 0.27	< 0.22	27	1.5	
845	23.67512	30.54024	5.43	-158	24.9 ± 4.2	2.1 ± 0.3	17.2 ± 3.6	11.3 ± 2.6	6.57 ± 0.12	30.8	0.84 ± 0.17	0.13 ± 0.03	3	1.3	291
846	23.67899	30.54273	5.50	-164	35.6 ± 9.6	2.0 ± 0.4	6.4 ± 1.7	14.1 ± 4.5	2.08 ± 0.08	15.5	< 0.46	< 0.22	73	3.2	291
847	23.67461	30.52941	5.51	-156	42.1 ± 7.6	2.1 ± 0.4	8.1 ± 1.5	18.7 ± 5.3	1.74 ± 0.09	11.9	< 0.26	< 0.15	-66	2.0	290
848	23.67362	30.51608	5.59	-155	36.6 ± 14.4	2.2 ± 0.3	9.2 ± 0.9	18.2 ± 5.2	3.10 ± 0.15	11.2	< 0.37	< 0.12	-75	1.2	253

NOTE— (1) ID number of the cloud. (2) – (3) $^{12}\text{CO}(J = 2 - 1)$ peak position of the cloud in equatorial coordinates (J2000) in degree. (4) Galactocentric radius of the cloud from the optical center of M33 ($1^{\text{h}}33^{\text{m}}50^{\text{s}}.9$, $30^{\circ}39'37''$) in units of kiloparsec. (5) Radial velocity in the Local Standard of Rest in units of km s^{-1} . (6) Deconvolved radius of the cloud including uncertainty in units of parsec. (7) Deconvolved velocity dispersion including uncertainty in units of km s^{-1} . (8) Luminosity mass based on $^{12}\text{CO}(J = 2 - 1)$ flux including uncertainty in units of $10^4 M_{\odot}$. (9) Mass of the cloud inferred from the virial theorem including uncertainty in units of $10^4 M_{\odot}$. (10) $^{12}\text{CO}(J = 2 - 1)$ intensity at its peak position of the cloud including uncertainty in units of K km s^{-1} . (11) S/N ratio of $^{12}\text{CO}(J = 2 - 1)$ brightness temperature at its peak position. (12) $^{13}\text{CO}(J = 2 - 1)$ intensity at $^{12}\text{CO}(J = 2 - 1)$ peak position of the cloud including uncertainty in units of K km s^{-1} , or its 3σ upper limit. (13) $^{13}\text{CO}(J = 2 - 1)/^{12}\text{CO}(J = 2 - 1)$ intensity ratio at $^{12}\text{CO}(J = 2 - 1)$ peak position of the cloud including uncertainty, or its 3σ upper limit. (14) Position angle of the major axis of the cloud, which is measured counterclockwise from north to east, in units of degree. (15) Ratio between the major and minor axes after the deconvolution by the observing beam ($7''.5$). (16) GMC counterpart identified with the IRAM 30 m telescope (Corbelli et al. 2017).

4.4. Basic Properties of Cataloged Molecular Clouds

Figure 8 shows the frequency distributions of the radius R and the velocity dispersion σ_v for the cataloged molecular clouds in M33. R ranges from 6.8 to 72 pc, and σ_v ranges from 1.0 to 6.1 km s⁻¹. Their medians are 34 pc and 2.8 km s⁻¹, respectively. Note that, as pointed out by Hughes et al. (2013), such distributions of the cloud radius and the velocity dispersion depend on both the spatial and the velocity resolutions of the input data cube because ISM in galaxies generally has a hierarchical structure from parsec to kiloparsec scales. We also examined the frequency distributions of M_{CO} and M_{Vir} as shown in Figure 9. M_{CO} ranges from 6.7×10^3 to $2.6 \times 10^6 M_\odot$, and M_{Vir} ranges from 1.1×10^4 to $1.9 \times 10^6 M_\odot$. Their medians are $9.9 \times 10^4 M_\odot$ and $2.8 \times 10^5 M_\odot$, respectively. Both for M_{CO} and M_{Vir} , the dynamic range of mass is more than two orders of magnitude, which is wider than earlier M33 studies (e.g., Rosolowsky et al. 2007; Gratier et al. 2012; Corbelli et al. 2017). The low-S/N (< 10) clouds typically show smaller radii and smaller velocity dispersions compared to the high-S/N clouds. However, some low-S/N clouds have large virial masses ($\geq 10^5 M_\odot$) although their CO luminosity masses are almost small ($< 10^5 M_\odot$). We discuss the origin of the discrepancy between M_{CO} and M_{Vir} for the low-S/N clouds in subsection 5.2.

5. SCALING RELATIONS

Starting with the pioneering work by Larson (1981), a lot of earlier studies suggest that basic properties of molecular clouds are quantitatively related to each other via some kind of scaling relations, which are often referred to as ‘‘Larson’s laws’’. In this section, we examine such scaling relations based on our molecular-cloud catalog.

5.1. Size–Line-width Relation

The first Larson’s law relates the cloud radius R in parsecs to the velocity dispersion σ_v in km s⁻¹, which is expressed as $\sigma_v = 0.72R^{0.5}$ for the MW (Solomon et al. 1987). This relation is considered to reflect the turbulent condition inside the molecular clouds. Figure 10 shows the relation between R and σ_v for 848 molecular clouds in M33, distinguishing the low-S/N and high-S/N clouds. The overall distributions in the radius-velocity dispersion plane are similar between the two cloud types; many clouds show smaller velocity dispersion than the Galactic $R - \sigma_v$ relation at a given radius regardless of the ¹²CO S/N ratio. This trend can be evaluated more quantitatively by deriving the coefficient of the $R - \sigma_v$ relation, $\sigma_v R^{0.5}$. The average $\sigma_v R^{0.5}$ for 848 clouds is

0.48 ± 0.13 , which is significantly smaller than the Galactic $\sigma_v R^{0.5}$, 0.72.

To explain the origin of such a smaller velocity dispersion, we examine the $R - \sigma_v$ relations based on the two earlier GMC catalogs in M33 (Rosolowsky et al. 2007; Corbelli et al. 2017). We found that the averaged $\sigma_v R^{0.5}$ are 0.54 ± 0.11 and 0.50 ± 0.17 for the Rosolowsky et al. (2007) catalog and the Corbelli et al. (2017) catalog, respectively, although the linewidth of small (< 20 pc) clouds in the Corbelli et al. (2017) catalog is comparable to the MW as pointed out by Braine et al. (2018). This suggests that the velocity dispersion of the GMC in M33 is intrinsically smaller than the Galactic GMCs.

Here, we consider the physical mechanism to change the velocity dispersion in molecular clouds. Earlier studies reported that the velocity dispersion at a given cloud radius is higher in the Galactic Center (Oka et al. 2001) and 30 Doradus in the LMC (Wong et al. 2017, 2019), which are associated with active star-forming regions, compared to the Galactic $R - \sigma_v$ relation (Solomon et al. 1987). In contrast to this, the quiescent cloud PGCC G282.92-32.40 (Planck Collaboration et al. 2016), which is referred to as the ‘‘Planck Cold Cloud (PCC)’’, in the LMC shows a smaller velocity dispersion than the Galactic $R - \sigma_v$ relation (Wong et al. 2017, 2019). From these observational facts, Wong et al. (2019) suggested that local energy injection by star formation feedback plays an important role in the turbulence of molecular clouds. In other words, it is unlikely that a molecular cloud without active star-forming regions increases its velocity dispersion. Considering that the $R - \sigma_v$ relation obtained in M33 is similar to that in the PCC, it is suggested that many molecular clouds in M33 are not associated with active star formation like the PCC. However, this contradicts the fact that more than 70% of clouds in M33 are associated with star-forming regions (e.g., Gratier et al. 2012; Konishi al. in preparation). Indeed, Figure 6 shows that many high-mass clouds are associated with 8 μ m-bright sources (see also Figure 15). Alternatively, Bolatto et al. (2008) examined the variation in $\sigma_v R^{0.5}$ for 12 external galaxies and found a trend that extragalactic GMCs falling under the Galactic $R - \sigma_v$ relation have lower surface densities (Σ_{GMC}) than corresponding clouds in the MW. GMCs in SMC and NGC 4605 show $\Sigma_{\text{GMC}} \sim 45$ and $\sigma_v R^{0.5} = 0.37$. Both values are lower than GMCs in other 10 external galaxies, while similar to those in M33 ($\Sigma_{\text{GMC}} = 30 - 40$ and $\sigma_v R^{0.5} = 0.4 - 0.5$). This suggests that low-surface density molecular clouds can be maintained even by the small turbulence (i.e., small velocity dispersion), which

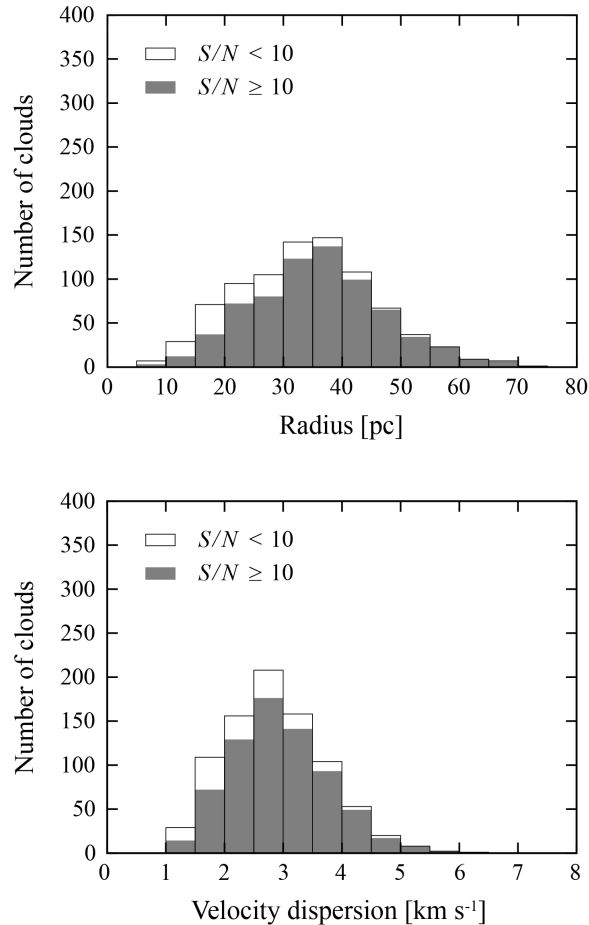


Figure 8. Frequency distributions of the radius (R ; top) and the velocity dispersion (σ_v ; bottom) for the cataloged molecular clouds in M33. A shaded column indicates high-S/N clouds and a white column corresponds to low-S/N clouds.

results in the observed $R - \sigma_v$ relation in M33 (see also Ohno et al. 2023).

5.2. CO Luminosity Mass–Virial Mass Relation

Figure 11 shows a relationship between M_{CO} and M_{Vir} for 848 molecular clouds in M33. Both masses seem to be well correlated, whereas M_{Vir} is generally larger than M_{CO} . A similar trend is also reported by Corbelli et al. (2017). In particular, the low-S/N clouds show larger M_{Vir} at a given M_{CO} ; the median of the virial parameter α , which is defined as $M_{\text{Vir}}/M_{\text{CO}}$, is 5.3 for the low-S/N clouds. Since clouds in virial equilibrium show $\alpha \approx 1 - 3$ (Miville-Deschênes et al. 2017), most of the low-S/N clouds are gravitationally unbound ($\alpha > 3$). On the other hand, the median of α for the high-S/N clouds is 2.0, and 68% of the high-S/N clouds are gravitationally bound ($\alpha \leq 3$). Considering that the $R - \sigma_v$ relation is not different between the high-S/N clouds and low-S/N clouds, the CO intensity emitted from the low-S/N cloud may be simply weak. This is consistent with the low-surface density molecular clouds in M33 (see subsection 5.1). In Figure 11, we can see most of the clouds

are virialized ($\alpha \leq 3$) at the high-mass end. We discuss the physical meaning of this trend in Section 7.

6. COMPARISON WITH EARLIER GMC CATALOG

Based on the ACA+IRAM $^{12}\text{CO}(J = 2 - 1)$ data of M33, we cataloged 848 molecular clouds. In this section, we compare the ACA+IRAM cloud catalog with the earlier GMC catalog generated by Corbelli et al. (2017). To give a fair comparison between the two catalogs, we extracted 362 GMCs from the Corbelli et al. (2017) catalog which are located within the ACA FOV. Hereafter, we refer to the GMCs in the Corbelli et al. (2017) catalog as “IRAM GMCs”. This comparison between the two catalogs provides new insights into the hierarchical structure of molecular gas.

6.1. Mass Function

Firstly, we investigate the cloud mass distributions for the two catalogs. The cumulative mass distribution function can be expressed by truncated power-law functions as follows:

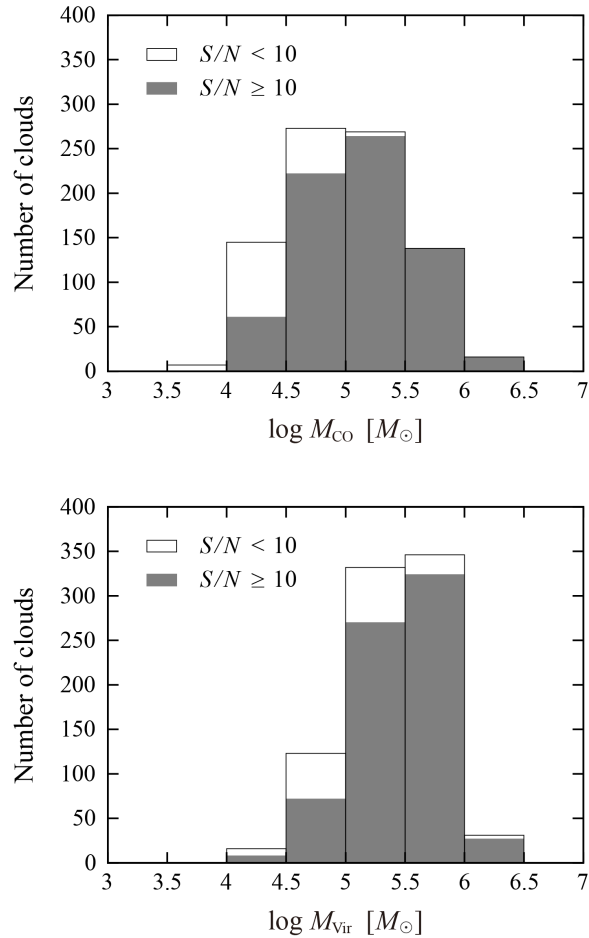


Figure 9. Frequency distributions of the ^{12}CO luminosity-based mass (M_{CO} ; top) and the virial mass (M_{vir} ; bottom) for the cataloged molecular clouds in M33. A shaded column indicates high-S/N clouds and a white column corresponds to low-S/N clouds.

$$N(M' > M) = N_0 \left[\left(\frac{M}{M_0} \right)^{\gamma+1} - 1 \right], \quad (4)$$

where M_0 is the maximum mass in the distribution, γ indicates how the cloud mass is distributed, and N_0 is the number of clouds more massive than $2^{1/(\gamma+1)}M_0$ (e.g., Rosolowsky 2005). To determine the fitting range of the cloud mass distributions, we estimated the completeness limit of molecular clouds by reference to Engargiola et al. (2003). They reported that the lowest mass molecular cloud in their GMC survey is of order $2 \times 10^4 M_{\odot}$ and also estimated the completeness limit of $1.5 \times 10^5 M_{\odot}$, which is about seven times larger than the lowest mass. If we apply such a linear scaling between the two masses to our molecular cloud catalog, the completeness limit is estimated to be $5 \times 10^4 M_{\odot}$ because the lowest mass cloud is $7 \times 10^3 M_{\odot}$ (see subsection 4.1). Note that we recalculated the GMC masses in

the Corbelli et al. (2017) catalog by assuming $R_{21} = 0.6$ and adopted $8.4 \times 10^4 M_{\odot}$ as the completeness limit².

Figure 12 shows the cumulative cloud mass functions fitted by the truncated power-law functions. Note that we treated N_0 as a free parameter (i.e., independent of γ) in this study to achieve the best fitting. We obtained $\gamma = -1.60$ for the ACA+IRAM cloud catalog and $\gamma = -1.48$ for the Corbelli et al. (2017) catalog, respectively. Considering that Braine et al. (2018) obtained $\gamma = -1.65$ for all 566 GMCs in the Corbelli et al. (2017) catalog, the cloud population of the ACA+IRAM cloud catalog is similar to that of the Corbelli et al. (2017) catalog. However, the truncated power-law fitting for the ACA+IRAM cloud catalog deviates from the mass spectrum at the high-mass side (especially from

² Corbelli et al. (2017) reported that the completeness limit is $6.3 \times 10^4 M_{\odot}$ in their GMC catalog. The assumption of $R_{21} = 0.6$ in this study yields the corrected completeness limit of $6.3 \times 10^4 \times (0.8/0.6) = 8.4 \times 10^4 M_{\odot}$.

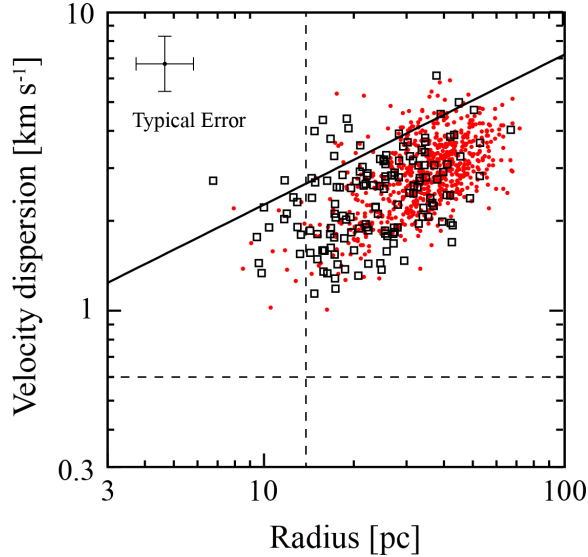


Figure 10. Radius-velocity dispersion ($R-\sigma_v$) relation for the molecular clouds in M33. Red dots indicate high-S/N clouds and open squares indicate low-S/N clouds. The solid line indicates the relation for the Galactic clouds ($\sigma_v = 0.72R^{0.5}$; Solomon et al. 1987). The dashed vertical and horizontal lines indicate the resolution limits obtained from the spatial and velocity resolutions of the ACA+IRAM $^{12}\text{CO}(J=2-1)$ data.

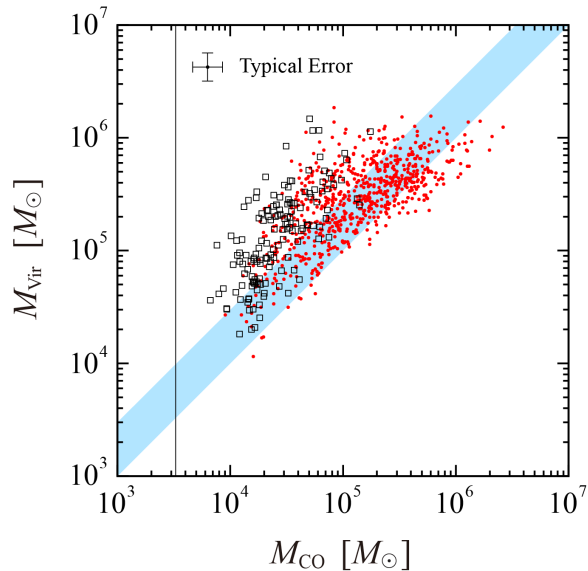


Figure 11. Comparison between the virial mass (M_{vir}) and the ^{12}CO luminosity-based mass (M_{CO}) for the molecular clouds in M33. Red dots indicate high-S/N clouds and open squares indicate low-S/N clouds. The filled area in blue indicates $1 \leq M_{\text{vir}}/M_{\text{CO}} \leq 3$, in which clouds are in virial equilibrium. The vertical line indicates the detection limit derived from the emission masks and PYCPROPS parameters.

$5 \times 10^5 M_{\odot}$ to $2 \times 10^6 M_{\odot}$); the number of clouds in this mass range is significantly less than the expectation by the truncated power-law function and also less than the Corbelli et al. (2017) catalog. Such a decrease in the high-mass clouds in the ACA+IRAM cloud catalog is presumably due to the difference in the spatial resolutions of CO data; some large IRAM GMCs identified with the 49 pc beam can be resolved into multi-

ple cloud components in the ACA+IRAM CO data at 30 pc resolution. This yields a decrease in the number of GMCs at the high-mass side. Indeed, we examined a one-on-one comparison between ACA+IRAM clouds and IRAM GMCs and found that 170 IRAM GMCs are resolved into 2 or more ACA+IRAM clouds. Figure 13 shows the comparison of the cloud identification between the two CO data. A small IRAM GMC is identified as

a single molecular cloud even in the ACA+IRAM CO data, while a large IRAM GMC are resolved into multiple ACA+IRAM clouds.

6.2. Origin of Velocity Dispersion in IRAM GMCs

As described above, a large IRAM GMC (typically its M_{CO} is larger than $3 \times 10^5 M_{\odot}$) can be treated as an association of multiple ACA+IRAM clouds. Investigating such a correspondence is beneficial for the comparison between properties of individual molecular clouds and the average properties of their association. In particular, we focus on the origin of the observed velocity dispersion (linewidth) of a large IRAM GMC, which is likely composed of two factors; (1) the line-of-sight relative velocity between internal ACA+IRAM clouds and (2) velocity dispersions of individual ACA+IRAM clouds. Here we examine which factors mainly contribute to the overall velocity dispersion for 77 IRAM GMCs, which are resolved into 3 or more ACA+IRAM clouds.

To quantify the line-of-sight velocity difference between multiple ACA+IRAM clouds, we firstly defined the weighted center of line-of-sight velocities between the clouds as follows:

$$v_g = \frac{\sum_{i=1}^n I_i v_i}{\sum_{i=1}^n I_i}, \quad (5)$$

where I_i and v_i are the $^{12}\text{CO}(J = 2 - 1)$ intensity at the CO peak position (10th column in Table 3) and the line-of-sight velocity (V_{LSR} ; 5th column in Table 3) of i th ACA+IRAM cloud, respectively. n is the number of ACA+IRAM clouds included in a large IRAM GMC. Using this v_g , we calculate the representative velocity difference between internal ACA+IRAM clouds as follows:

$$v_{\text{diff}} = \sqrt{\frac{\sum_{i=1}^n I_i (v_i - v_g)^2}{\sum_{i=1}^n I_i}}. \quad (6)$$

In addition, we calculate the weighted mean of velocity dispersions of individual ACA+IRAM clouds as follows:

$$\sigma_{v,\text{mean}} = \frac{\sum_{i=1}^n I_i \sigma_{v,i}}{\sum_{i=1}^n I_i}, \quad (7)$$

where $\sigma_{v,i}$ is the velocity dispersion of i th ACA+IRAM cloud.

Figure 14 shows the velocity dispersion of the IRAM GMC as a function of v_{diff} and that of $\sigma_{v,\text{mean}}$. A clear correlation between v_{diff} and the velocity dispersion of the IRAM GMC, with the Spearman's rank correlation coefficient r_s of 0.59, can be seen, while $\sigma_{v,\text{mean}}$ seems nearly constant ($2-4 \text{ km s}^{-1}$) and its correlation with the velocity dispersion of the IRAM GMC is weak ($r_s = 0.28$). This suggests that the velocity dispersion of a large cloud is mainly dominated by the line-of-sight velocity difference between small clouds inside the GMC in the case of $v_{\text{diff}} > 2 \text{ km s}^{-1}$, while the velocity dispersion of individual internal clouds determines the overall velocity dispersion of the GMC if v_{diff} is less than 2 km s^{-1} .

7. PROPERTIES OF MOLECULAR CLOUDS AND HIGH-MASS STAR FORMATION

As shown in Figure 6 (and also described in subsection 4.1), many high-mass clouds are associated with the strong $8 \mu\text{m}$ emission in the spiral arm region, while low-mass clouds tend to be apart from such $8 \mu\text{m}$ -bright sources and to exist in the inter-arm region. Here, we quantitatively evaluate the relationship between the molecular clouds and the $8 \mu\text{m}$ -bright sources. To do this, we regridded the IRAC $8 \mu\text{m}$ map (Dale et al. 2009) to match the ACA+IRAM $^{12}\text{CO}(J = 2 - 1)$ map and obtained mean $8 \mu\text{m}$ flux by averaging the pixel values included within each molecular cloud. Then, we constructed the cumulative distribution functions (CDFs) both for 423 high-mass clouds and 425 low-mass clouds. Figure 15 clearly shows that the $8 \mu\text{m}$ -bright sources are closely associated with high-mass clouds rather than low-mass clouds; the strong ($> 2 \text{ MJy sr}^{-1}$) $8 \mu\text{m}$ emission is found in 72% of high-mass clouds, but only in 36% of low-mass clouds, respectively. Note that this trend does not change even if we exclude the diffuse components of $8 \mu\text{m}$ emission (see appendix). Our result indicates that high-mass star formation tends to be associated with high-mass clouds rather than low-mass clouds. Such a trend is consistent with the extensive study by Corbelli et al. (2017); they identified mid-infrared (MIR) emission with GMCs and found that a GMC with bright MIR sources tends to have a large CO luminosity mass.

Since high-mass star formation generally starts from the gravitational instability of molecular gas, the virial parameter α , which expresses the degree of gravitational binding, is useful to examine star formation in molecular clouds. Figure 16 shows α as a function of M_{CO} for each ACA+IRAM cloud in M33. α generally decreases (i.e., becomes more unstable against gravitational collapse) with the increase in M_{CO} . A similar trend is

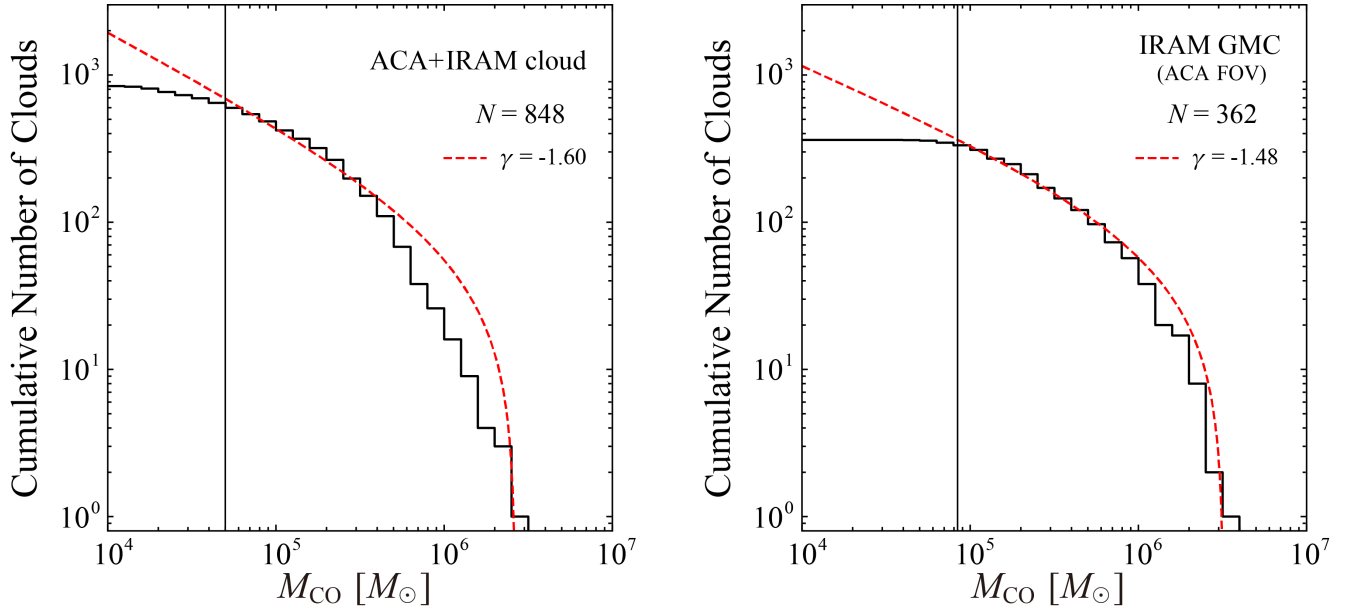


Figure 12. Cumulative cloud mass functions from the ACA+IRAM catalog (left) and the Corbelli et al. (2017) catalog (right). The red dashed lines indicate the fitting results by the truncated power-law functions. The vertical lines show the completeness limit in each plot.

also observed in the MW (e.g., Miville-Deschênes et al. 2017) and external galaxies (IC 342; Hirota et al. 2011). In M33, high-mass clouds whose mass is larger than $10^5 M_{\odot}$ seem to be almost virialized; in other words, the self-gravitation is predominant rather than the internal turbulence of the cloud. This indicates that the high-mass star formation likely onsets within such high-mass clouds by the gravitational instability, which is well consistent with the observed feature; many high-mass clouds are associated with $8 \mu\text{m}$ -bright sources (Figures 6 and 15). In addition, a large α for the low-S/N clouds with a median of 5.3 can be explained; the low-S/N clouds largely correspond to low-mass clouds, which are gravitationally unbound and not associated with star-forming regions.

Finally, we briefly discuss the evolution of molecular clouds. In M33, many high-mass clouds exist in the spiral arm region, while the inter-arm region is dominated by low-mass clouds. Since the $8 \mu\text{m}$ -bright sources are loosely along spiral arms in M33, the stellar potential may play a vital role in the accumulation (and the resultant mass growth) of molecular clouds. The evolution of molecular clouds crossing the spiral arm and the high-mass star formation within them are often discussed for grand-design spiral galaxies such as M51 (Egusa et al. 2011) and IC 342 (Hirota et al. 2011) based on the interferometric CO($J = 1 - 0$) observations at a spatial resolution of a few $\times 10$ pc. In M51, Egusa et al. (2011) suggested that smaller molecular clouds collide to form smooth giant molecular associations (GMAs) at spiral

arm regions and then star formation is triggered in the GMA cores. Hirota et al. (2011) divided the GMCs in the spiral arm of IC 342 into two categories according to whether they are associated with star formation activity or not, and reported that the GMCs with H II regions are typically more virialized and massive compared to the GMCs without H II regions. These results are consistent with the picture of molecular clouds and the high-mass star formation in M33 although it is a flocculent galaxy whose spiral arm structures are relatively weak. In a forthcoming paper, we will report a detailed study on the evolutionary stage of GMCs based on the comparison with H II regions (Konishi et al. in preparation). Although the GMC evolution in M33 was investigated in earlier studies (e.g., Miura et al. 2012; Corbelli et al. 2017), the new ACA CO($J = 2 - 1$) data enable us to study the dense-gas formation based on ^{13}CO ($J = 2 - 1$) emission as well as the evolution of basic properties of clouds (e.g., size, linewidth, mass, and virial parameters).

8. SUMMARY

We have performed ALMA-ACA 7-m-array observations in ^{12}CO ($J = 2 - 1$), ^{13}CO ($J = 2 - 1$), and C^{18}O ($J = 2 - 1$) line emission toward the molecular-gas disk in M33 at an angular resolution of $7''.31 \times 6''.50$ ($30 \text{ pc} \times 26 \text{ pc}$). We combined the ACA 7-m-array ^{12}CO ($J = 2 - 1$) data with the IRAM 30m data to compensate for diffuse molecular-gas components. The summary of this work is as follows:

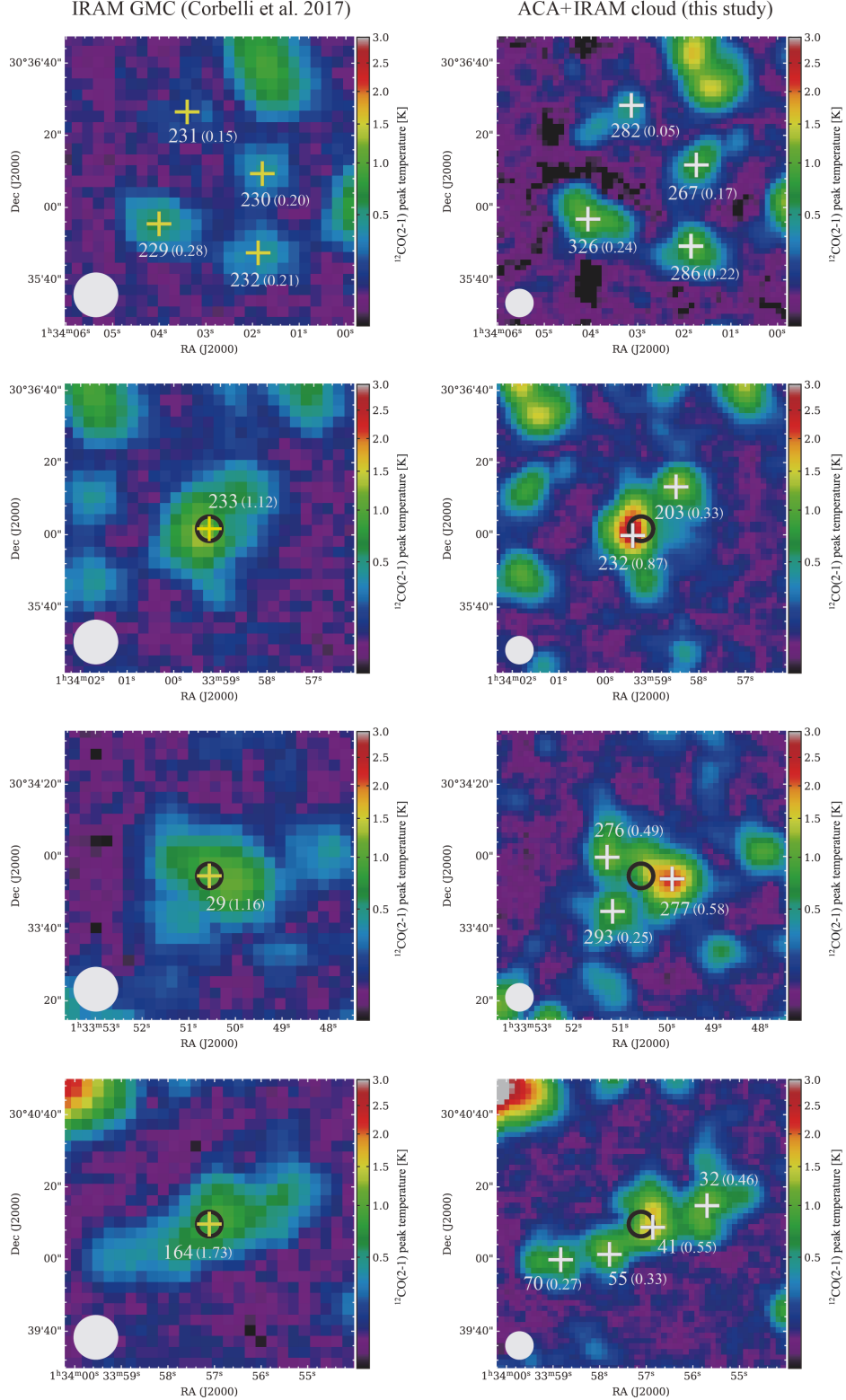


Figure 13. Comparison of the cloud identification between IRAM GMCs (left) and ACA+IRAM clouds (right) in $^{12}\text{CO}(J=2-1)$ peak temperature maps. Yellow crosses and black circles indicate $^{12}\text{CO}(J=2-1)$ peak positions in each IRAM GMCs. White crosses indicate $^{12}\text{CO}(J=2-1)$ peak positions in each ACA+IRAM cloud. Numbers in the left column correspond to GMC IDs in the IRAM GMC catalog (Corbelli et al. 2017), and those in the right column are cloud IDs in the ACA+IRAM cloud catalog (Table 3). The value in parentheses after the ID indicates M_{CO} in units of $10^6 M_{\odot}$ for each cloud. The beam size is shown in the lower left corner of each map.

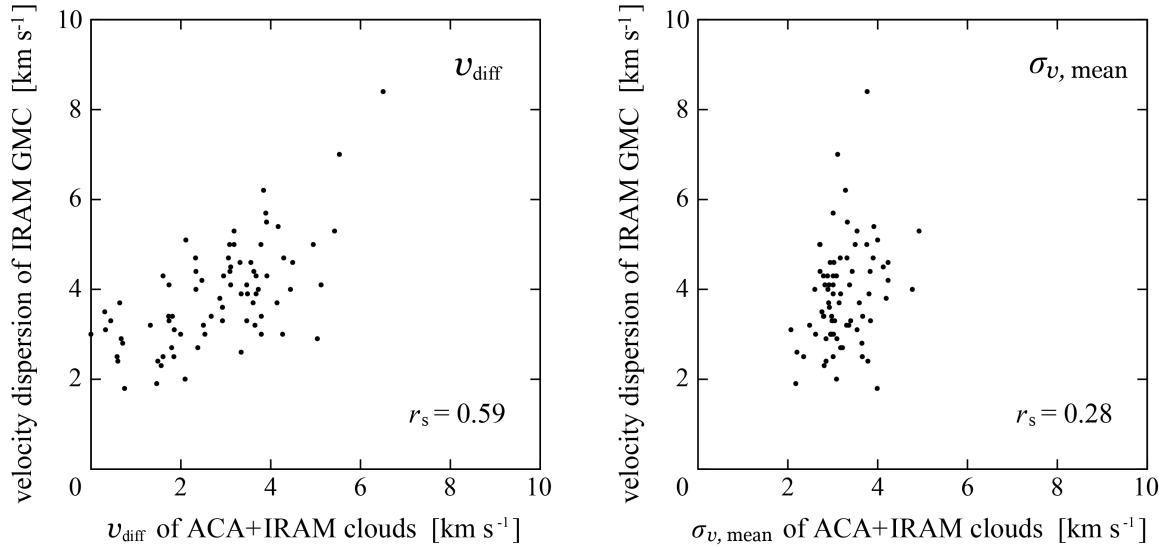


Figure 14. Velocity dispersion of the IRAM GMC as a function of the representative line-of-sight velocity difference between internal ACA+IRAM clouds v_{diff} (left) and that of the weighted mean of velocity dispersions of individual ACA+IRAM clouds $\sigma_{v,\text{mean}}$ (right). The Spearman’s rank correlation coefficient r_s is shown in the bottom-right corner of each plot.

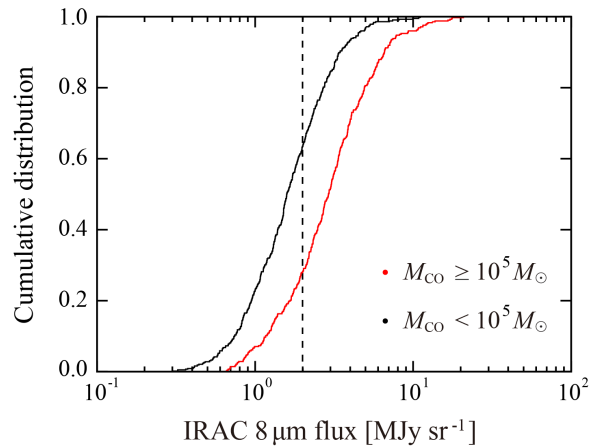


Figure 15. Normalized CDF of mean $8\mu\text{m}$ flux in each molecular cloud. The red and black lines indicate the CDF for 423 high-mass clouds ($M_{\text{CO}} \geq 10^5 M_{\odot}$) and 425 low-mass clouds ($M_{\text{CO}} < 10^5 M_{\odot}$), respectively. The vertical dashed line indicates the $8\mu\text{m}$ flux of 2 MJy sr^{-1} .

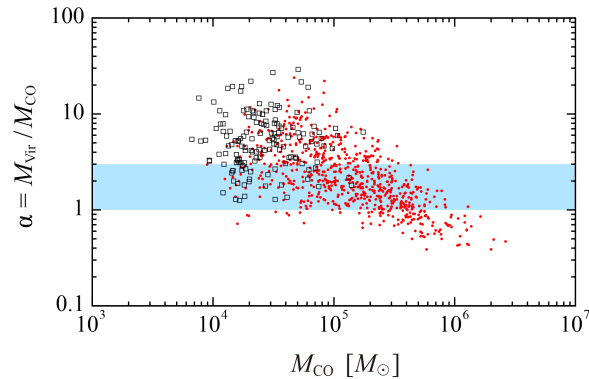


Figure 16. Virial parameter α as a function of the ^{12}CO luminosity-based mass (M_{CO}). The filled area in blue indicates $1 \leq \alpha \leq 3$, in which clouds are in virial equilibrium. Red dots indicate high-S/N clouds and open squares indicate low-S/N clouds.

1. The ACA+IRAM combined $^{12}\text{CO}(J = 2 - 1)$ map clearly depicts the cloud-scale molecular-gas struc-

ture over the M33 disk. In addition, we detected

- a lot of $^{13}\text{CO}(J = 2 - 1)$ sources which correspond to moderately dense molecular gas.
2. We decomposed individual cloud components from the ACA+IRAM $^{12}\text{CO}(J = 2 - 1)$ cube data employing PYCPROPS, and cataloged 848 molecular clouds with a mass range from $10^3 M_{\odot}$ to $10^6 M_{\odot}$. We found that high-mass clouds ($M_{\text{CO}} \geq 10^5 M_{\odot}$) tend to associate with the $8 \mu\text{m}$ -bright sources in the spiral arm region, while low-mass clouds ($M_{\text{CO}} < 10^5 M_{\odot}$) tend to be apart from such $8 \mu\text{m}$ -bright sources and to exist in the inter-arm region.
 3. We found that most of the molecular clouds in M33 show smaller velocity dispersions than the Galactic $R - \sigma_v$ relation at a given radius. This is presumably due to low-surface density molecular clouds, which may be maintained even by the small turbulence.
 4. We found that a small IRAM GMC is identified as a single molecular cloud even in ACA+IRAM CO data, while a large IRAM GMC (typically its M_{CO} is larger than $3 \times 10^5 M_{\odot}$) can be resolved into multiple ACA+IRAM clouds. The velocity dispersion of a large IRAM GMC is mainly dominated by the line-of-sight velocity difference between small clouds inside the GMC rather than the internal cloud velocity broadening.
 5. Based on the comparison between M_{CO} and M_{Vir} for ACA+IRAM clouds, we found that high-mass

clouds in M33 are almost virialized. This indicates that the high-mass star formation likely onsets within such high-mass clouds by the gravitational instability.

We thank the anonymous referee for helpful comments, which significantly improved the manuscript. This paper makes use of the following ALMA data: [ADS/JAO.ALMA#2017.1.00461.S](#) [ADS/JAO.ALMA#2018.A.00058.S](#) [ADS/JAO.ALMA#2017.1.009](#) and [ADS/JAO.ALMA#2019.1.01182.S](#) ALMA is a partnership of ESO (representing its member states), NSF (USA) and NINS (Japan), together with NRC (Canada), NSC and ASIAA (Taiwan), and KASI (Republic of Korea), in cooperation with the Republic of Chile. The Joint ALMA Observatory is operated by ESO, AUI/NRAO, and NAOJ. This work is based on observations made with the *Spitzer Space Telescope*, which is operated by the Jet Propulsion Laboratory, California Institute of Technology, under a contract with NASA. Data analysis was in part carried out on the Multi-wavelength Data Analysis System operated by the Astronomy Data Center (ADC), National Astronomical Observatory of Japan. This work was supported by NAOJ ALMA Scientific Research grant Nos. 2022-22B and JSPS KAKENHI (grant Nos. JP18H05440, JP21H00049, and JP21K13962).

Software: CASA (v5.4.0; [McMullin et al. 2007](#)), Astropy ([Astropy Collaboration et al. 2018](#)), APLpy (v1.1.1; [Robitaille & Bressert 2012](#))

APPENDIX

A. DIFFUSE EMISSION SUBTRACTION FOR IRAC $8 \mu\text{m}$ DATA

In Section 7, we measured $8 \mu\text{m}$ flux as a proxy for star formation activity in M33. Generally, star formation rates (SFRs) are estimated from $\text{H}\alpha$ (and also far-infrared emission such as $24 \mu\text{m}$) luminosities by assuming that all the $\text{H}\alpha$ emitting gas is ionized by the local star-forming region. Although the typical size of an H II region is $\sim 0.1 - 10 \text{ pc}$ in the MW (e.g., [Kennicutt 1984](#); [Garay & Lizano 1999](#)), $\text{H}\alpha$ maps for nearby galaxies often show 100 pc scale (or more) ionizing gas distributions. The theoretical studies showed that clumpy density structures of ISM allow for larger escape fractions of ionizing radiation (e.g., [Haffner et al. 2009](#), and references therein). This indicates that the $\text{H}\alpha$ emitting gas is not necessarily ionized by the local star-forming region, and thus the diffuse components of $\text{H}\alpha$ emission should be considered for the estimation of SFRs. Such diffuse components are also observed in the IRAC $8 \mu\text{m}$ map that we used.

To extract the compact $8 \mu\text{m}$ emission which directly reflects the star formation from the diffuse components, we applied *HIIphot*, an IDL software developed by [Thilker et al. \(2000\)](#). Following the procedures in [Liu et al. \(2011\)](#), we subtracted the diffuse components from the $8 \mu\text{m}$ map. Figure 17 shows the same as Figure 15, but using the $8 \mu\text{m}$ flux without diffuse components. The general trend found in Figure 15 does not change; the $8 \mu\text{m}$ -bright sources are closely associated with high-mass clouds rather than low-mass clouds.

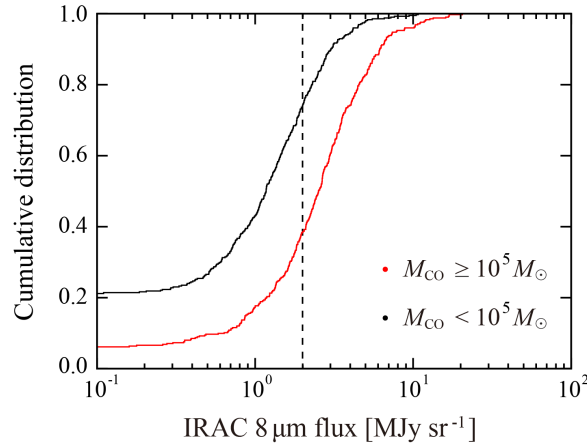


Figure 17. Same as Figure 15, but using the 8 μm flux without diffuse components.

REFERENCES

- Astropy Collaboration, Price-Whelan, A. M., Sipőcz, B. M., et al. 2018, *AJ*, 156, 123
- Braine, J., Rosolowsky, E., Gratier, P., et al. 2018, *A&A*, 612, A51. doi:10.1051/0004-6361/201732405
- Bolatto, A. D., Leroy, A. K., Rosolowsky, E., et al. 2008, *ApJ*, 686, 948. doi:10.1086/591513
- Bolatto, A. D., Wolfire, M., & Leroy, A. K. 2013, *ARA&A*, 51, 207. doi:10.1146/annurev-astro-082812-140944
- Calzetti, D., Kennicutt, R. C., Bianchi, L., et al. 2005, *ApJ*, 633, 871. doi:10.1086/466518
- Calzetti, D., Kennicutt, R. C., Engelbracht, C. W., et al. 2007, *ApJ*, 666, 870. doi:10.1086/520082
- Cao, Y., Wong, T., Xue, R., et al. 2017, *ApJ*, 847, 33. doi:10.3847/1538-4357/aa88c5
- Cao, Y., Wong, T., Bolatto, A. D., et al. 2023, arXiv:2306.07640. doi:10.48550/arXiv.2306.07640
- Colombo, D., Hughes, A., Schinnerer, E., et al. 2014, *ApJ*, 784, 3. doi:10.1088/0004-637X/784/1/3
- Corbelli, E., Braine, J., Bandiera, R., et al. 2017, *A&A*, 601, A146. doi:10.1051/0004-6361/201630034
- Corbelli, E., Thilker, D., Zibetti, S., et al. 2014, *A&A*, 572, A23. doi:10.1051/0004-6361/201424033
- Cormier, D., Bigiel, F., Jiménez-Donaire, M. J., et al. 2018, *MNRAS*, 475, 3909. doi:10.1093/mnras/sty059
- Crocker, A. F., Calzetti, D., Thilker, D. A., et al. 2013, *ApJ*, 762, 79. doi:10.1088/0004-637X/762/2/79
- Dale, D. A., Cohen, S. A., Johnson, L. C., et al. 2009, *ApJ*, 703, 517. doi:10.1088/0004-637X/703/1/517
- den Brok, J. S., Bigiel, F., Sliwa, K., et al. 2022, *A&A*, 662, A89. doi:10.1051/0004-6361/202142247
- den Brok, J. S., Chatzigiannakis, D., Bigiel, F., et al. 2021, *MNRAS*, 504, 3221. doi:10.1093/mnras/stab859
- Druard, C., Braine, J., Schuster, K. F., et al. 2014, *A&A*, 567, A118. doi:10.1051/0004-6361/201423682
- Egusa, F., Koda, J., & Scoville, N. 2011, *ApJ*, 726, 85. doi:10.1088/0004-637X/726/2/85
- Engargiola, G., Plambeck, R. L., Rosolowsky, E., et al. 2003, *ApJS*, 149, 343. doi:10.1086/379165
- Freedman, W. L., Wilson, C. D., & Madore, B. F. 1991, *ApJ*, 372, 455. doi:10.1086/169991
- Fukui, Y., Kawamura, A., Minamidani, T., et al. 2008, *ApJS*, 178, 56. doi:10.1086/589833
- Fukui, Y., Mizuno, N., Yamaguchi, R., et al. 1999, *PASJ*, 51, 745. doi:10.1093/pasj/51.6.745
- Galletti, S., Bellazzini, M., & Ferraro, F. R. 2004, *A&A*, 423, 925. doi:10.1051/0004-6361:20040489
- Garay, G. & Lizano, S. 1999, *PASP*, 111, 1049. doi:10.1086/316416
- Gratier, P., Braine, J., Rodriguez-Fernandez, N. J., et al. 2010, *A&A*, 522, A3. doi:10.1051/0004-6361/201014441
- Gratier, P., Braine, J., Rodriguez-Fernandez, N. J., et al. 2012, *A&A*, 542, A108. doi:10.1051/0004-6361/201116612
- Gratier, P., Braine, J., Schuster, K., et al. 2017, *A&A*, 600, A27. doi:10.1051/0004-6361/201629300
- Haffner, L. M., Dettmar, R.-J., Beckman, J. E., et al. 2009, *Reviews of Modern Physics*, 81, 969. doi:10.1103/RevModPhys.81.969
- Hirota, A., Kuno, N., Sato, N., et al. 2010, *PASJ*, 62, 1261. doi:10.1093/pasj/62.5.1261
- Hirota, A., Kuno, N., Sato, N., et al. 2011, *ApJ*, 737, 40. doi:10.1088/0004-637X/737/1/40
- Hughes, A., Meidt, S. E., Colombo, D., et al. 2013, *ApJ*, 779, 46. doi:10.1088/0004-637X/779/1/46
- Kawamura, A., Mizuno, Y., Minamidani, T., et al. 2009, *ApJS*, 184, 1. doi:10.1088/0067-0049/184/1/1

- Kennicutt, R. C. 1984, *ApJ*, 287, 116. doi:10.1086/162669
- Kepley, A. A., Tsutsumi, T., Brogan, C. L., et al. 2020, *PASP*, 132, 024505
- Kobayashi, M. I. N., Inutsuka, S.-. ichiro ., Kobayashi, H., et al. 2017, *ApJ*, 836, 175. doi:10.3847/1538-4357/836/2/175
- Kobayashi, M. I. N., Kobayashi, H., Inutsuka, S.-. ichiro ., et al. 2018, *PASJ*, 70, S59. doi:10.1093/pasj/psy018
- Koch, E. W., Rosolowsky, E. W., Lockman, F. J., et al. 2018, *MNRAS*, 479, 2505. doi:10.1093/mnras/sty1674
- Kondo, H., Tokuda, K., Muraoka, K., et al. 2021, *ApJ*, 912, 66. doi:10.3847/1538-4357/abeb65
- Konishi, A., Muraoka, K., Tokuda, K., et al. 2023, *ApJ*, in prep.
- Larson, R. B. 1981, *MNRAS*, 194, 809. doi:10.1093/mnras/194.4.809
- Leroy, A. K., Rosolowsky, E., Usero, A., et al. 2022, *ApJ*, 927, 149. doi:10.3847/1538-4357/ac3490
- Leroy, A. K., Schinnerer, E., Hughes, A., et al. 2021, *ApJS*, 257, 43. doi:10.3847/1538-4365/ac17f3
- Liu, G., Koda, J., Calzetti, D., et al. 2011, *ApJ*, 735, 63. doi:10.1088/0004-637X/735/1/63
- Massey, Philip, Olsen, K. A. G., Hodge, Paul W., et al. 2006, *AJ*, 131, 5. doi:10.1086/503256
- Massey, Philip, McNeill, Reagin T., Olsen, K. A. G., et al. 2007, *AJ*, 134, 6. doi:10.1086/523658
- McMullin, J. P., Waters, B., Schiebel, D., et al. 2007, *Astronomical Data Analysis Software and Systems XVI*, 127
- Miura, R. E., Kohno, K., Tosaki, T., et al. 2012, *ApJ*, 761, 37. doi:10.1088/0004-637X/761/1/37
- Miura, R. E., Kohno, K., Tosaki, T., et al. 2014, *ApJ*, 788, 167. doi:10.1088/0004-637X/788/2/167
- Miville-Deschênes, M.-A., Murray, N., & Lee, E. J. 2017, *ApJ*, 834, 57. doi:10.3847/1538-4357/834/1/57
- Morokuma-Matsui, K., Sorai, K., Sato, Y., et al. 2020, *PASJ*, 72, 90. doi:10.1093/pasj/psaa084
- Muraoka, K., Sorai, K., Kuno, N., et al. 2016, *PASJ*, 68, 89. doi:10.1093/pasj/psw080
- Muraoka, K., Kondo, H., Tokuda, K., et al. 2020, *ApJ*, 903, 94. doi:10.3847/1538-4357/abb822
- Ohno, T., Tokuda, K., Konishi, A., et al. 2023, *ApJ*, 949, 63. doi:10.3847/1538-4357/accadb
- Oka, T., Hasegawa, T., Sato, F., et al. 2001, *ApJ*, 562, 348. doi:10.1086/322976
- Onodera, S., Kuno, N., Tosaki, T., et al. 2010, *ApJL*, 722, L127. doi:10.1088/2041-8205/722/2/L127
- Onodera, S., Kuno, N., Tosaki, T., et al. 2012, *PASJ*, 64, 133. doi:10.1093/pasj/64.6.133
- Paglione, T. A. D., Wall, W. F., Young, J. S., et al. 2001, *ApJS*, 135, 183. doi:10.1086/321785
- Pety, J., Schinnerer, E., Leroy, A. K., et al. 2013, *ApJ*, 779, 43. doi:10.1088/0004-637X/779/1/43
- Planck Collaboration, Ade, P. A. R., Aghanim, N., et al. 2016, *A&A*, 594, A28. doi:10.1051/0004-6361/201525819
- Robitaille, T., & Bressert, E. 2012, *APLpy: Astronomical Plotting Library in Python*, ascl:1208.017
- Rosolowsky, E. 2005, *PASP*, 117, 1403. doi:10.1086/497582
- Rosolowsky, E., Hughes, A., Leroy, A. K., et al. 2021, *MNRAS*, 502, 1218. doi:10.1093/mnras/stab085
- Rosolowsky, E., Keto, E., Matsushita, S., et al. 2007, *ApJ*, 661, 830. doi:10.1086/516621
- Rosolowsky, E. & Leroy, A. 2006, *PASP*, 118, 590. doi:10.1086/502982
- Rosolowsky, E. W., Pineda, J. E., Kauffmann, J., et al. 2008, *ApJ*, 679, 1338. doi:10.1086/587685
- Sanders, D. B., Scoville, N. Z., & Solomon, P. M. 1985, *ApJ*, 289, 373. doi:10.1086/162897
- Sano, H., Tsuge, K., Tokuda, K., et al. 2021, *PASJ*, 73, S62. doi:10.1093/pasj/psaa045
- Schinnerer, E., Meidt, S. E., Pety, J., et al. 2013, *ApJ*, 779, 42. doi:10.1088/0004-637X/779/1/42
- Skrutskie, M. F., Cutri, R. M., Stiening, R., et al. 2006, *AJ*, 131, 1163. doi:10.1086/498708
- Solomon, P. M., Rivolo, A. R., Barrett, J., et al. 1987, *ApJ*, 319, 730. doi:10.1086/165493
- Thilker, D. A., Braun, R., & Walterbos, R. A. M. 2000, *AJ*, 120, 3070. doi:10.1086/316852
- Tokuda, K., Kondo, H., Ohno, T., et al. 2021, *ApJ*, 922, 171. doi:10.3847/1538-4357/ac1ff4
- Tokuda, K., Muraoka, K., Kondo, H., et al. 2020, *ApJ*, 896, 36. doi:10.3847/1538-4357/ab8ad3
- Topal, S. 2020, *MNRAS*, 495, 2682. doi:10.1093/mnras/staa1146
- Tosaki, T., Kuno, N., Onodera, S. M., et al. 2011, *PASJ*, 63, 1171. doi:10.1093/pasj/63.6.1171
- Watanabe, Y., Sorai, K., Kuno, N., et al. 2011, *MNRAS*, 411, 1409. doi:10.1111/j.1365-2966.2010.17746.x
- Wong, T., Hughes, A., Tokuda, K., et al. 2017, *ApJ*, 850, 139. doi:10.3847/1538-4357/aa9333
- Wong, T., Hughes, A., Tokuda, K., et al. 2019, *ApJ*, 885, 50. doi:10.3847/1538-4357/ab46ba
- Wu, H., Cao, C., Hao, C.-N., et al. 2005, *ApJL*, 632, L79. doi:10.1086/497961
- Yajima, Y., Sorai, K., Kuno, N., et al. 2019, *PASJ*, 71, S13. doi:10.1093/pasj/psz022
- Yajima, Y., Sorai, K., Miyamoto, Y., et al. 2021, *PASJ*, 73, 257. doi:10.1093/pasj/psaa119

Yoda, T., Handa, T., Kohno, K., et al. 2010, PASJ, 62,
1277. doi:10.1093/pasj/62.5.1277